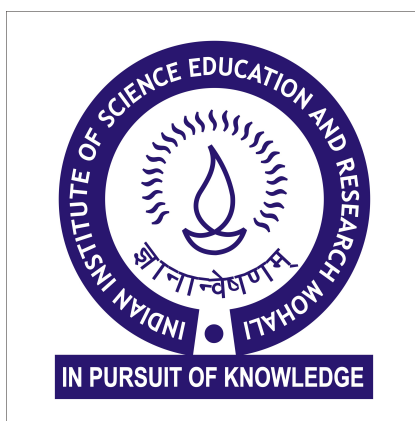


To Mitigate the Effect of Moonlight Contamination in Spectroscopic Searches for Extrasolar Planets

Komal Bali

*A dissertation submitted for the partial fulfilment of BS-MS dual degree in
Science*



Indian Institute of Science Education and Research, Mohali

May 2023

Certificate of Examination

This is to certify that the dissertation titled **To mitigate the effect of moonlight contamination in spectroscopic searches for extrasolar planets** submitted by **Komal Bali** (Reg. No. MS18192) for the partial fulfillment of BS- MS Dual Degree program of the institute, has been examined by the thesis committee duly appointed by the institute. The committee finds the work done by the candidate satisfactory and recommends that the report be accepted.

Prof. Harvinder Kaur Jassal

Dr. Pankaj Kushwaha

Prof Jasjeet Singh Bagla
(Co-Supervisor)

Dr. Joe Philip Ninan
(Supervisor)

Dated: May 1st, 2023

Declaration

The work presented in this dissertation has been carried out by me under the guidance of Dr. Joe Philip Ninan at the Tata Institute of Fundamental Research, Mumbai & Smithsonian and Prof. Jasjeet Singh Bagla at the Indian Institute of Science Education and Research, Mohali.

This work has not been submitted in part or in full for a degree, a diploma, or a fellowship to any other university or institute. Whenever contributions of others are involved, every effort is made to indicate this clearly, with due acknowledgement of collaborative research and discussions. This thesis is a bonafide record of original work done by me and all sources listed within have been detailed in the bibliography.

[Komal Bali]

(Candidate)

Dated: [1st May, 2023]

In my capacity as the supervisor of the candidates project work, I certify that the above statements by the candidate are true to the best of my knowledge.

[Prof Jasjeet Singh Bagla]

(Supervisor)

Dated: [1st May, 2023]

Acknowledgements

Firstly, I would like to thank the Supreme Power – God/Universe/Nature for blessing me and giving me the strength to reach till here that I am about to graduate. I am extremely thankful to Dr. Joe Philip Ninan for guiding me throughout this project with utmost support. Working remotely for more than a semester was not easy, but I am thankful to Joe for regularly communicating via Zoom meetings, Slack messages and emails. Joe made sure that I had my fundamentals clear and also am delving into the details of the field. There were times when I had silly doubts and times when I was stressed. But Joe motivated and encouraged me to overcome my fears and enjoy the science I am doing. I am grateful to Joe for pushing me to submit abstracts for multiple conferences which I also attended during my thesis year. I am also thankful to Joe for inviting me to visit TIFR Mumbai to enjoy the benefits of working offline and for making sure that the stay was helpful to me.

I warmly extend my gratitude to Prof. Jasjeet Singh Bagla who is my local supervisor. For the last 3 years, he has been my mentor and has played a key role in uplifting me and guiding me to the right path and opportunities. His interactions in weekly meetings, suggestions and support helped me a lot. Also a coincidence: when I took the IISER Aptitude Test, Prof. Bagla signed my hall ticket. Little did I know back then that he will also be signing my Master's thesis as a supervisor!

Next, I am thankful to my committee members Prof. Harvinder Kaur Jassal and Dr. Pankaj Kushwaha, who not only gave suggestions during my project and clarified my concepts, but also motivated me to share my work confidently and gave tips on how to analyse and present my data better. I am thankful to Dr. Arpita Roy who gave me the opportunity to work on this amazing project and kept supporting me throughout by checking with me on my progress regularly. I also thank Prof. Suvrath Mahadevan for his suggestions and guidance on important aspects of the project. I am extremely thankful to Arvind Gupta, whose 'brightness tool' gave the initial push I needed with this project. I also thank Dr. Nestor Espinoza for the funding support. I would also thank some of my other undergraduate mentors like Prof N.G. Prasad, Dr. Abhishek Chaudhuri, Dr. Caitlin Ahrens, Dr. Jason Soderblom who inspired me and kept a check on me to become a better researcher.

Last but not the least, I am indebted to my parents for always rooting for me and taking care of me in every way so that I become better every day in not just my profession but also as a human being. Without their support, I wouldn't have reached this stage in my life. My brother Ranjan also owes a big thanks for making me forget my stress and engaging me in fun and always wishing me good luck for my work. I thank Anshuman and Achuthan for their valuable suggestions to my thesis journey and IISER journey as a whole, not only as seniors but also as good friends. And I thank all my other friends who kept me sane in this process!

Abstract

Radial velocity (RV) exoplanet detection is undergoing an ongoing race to reach higher and higher levels of precision, motivated by the need to detect Earth-mass planets in the habitable zone. Lunar and atmospheric scattering of sunlight, which results in systematic errors in stellar radial velocity (RV) measurements, can significantly degrade the 10 cm s^{-1} sensitivity required to detect and characterize terrestrial exoplanets in or near habitable zones of Sun-like stars. With mask-based or template-based cross-correlation techniques, the addition of low-level spectral contamination introduces systematic noise into the velocity measurements.

The NEID (NN-EXPLORE Exoplanet Investigations with Doppler spectroscopy) precision RV instrument for the WIYN (Wisconsin-Indiana-Yale-NOIRLab) 3.5 m telescope serves as an ongoing resource for the community to explore and evaluate correction techniques. For these next-generation instruments to achieve 10 cm s^{-1} precision on the most interesting exoplanet systems, dark skies may be required, even though “bright time” has traditionally sufficed for RV science. Dr. Arpita Roy at STScI had worked on the simulations to minimize solar contamination’s impact to very low levels before the NEID spectrograph started taking data.

I worked on radial velocity data taken by the NEID Spectrograph to estimate the range of RV measurement error induced by scattered sunlight contamination as compared to the predictions in [Roy 20]. I demonstrate the effectiveness of different correction techniques, using simultaneous spectrometer sky fibers that are expected to reduce this source of error to below the photon-noise limit of typical stellar observations. I worked to verify the assumptions of the previously done simulations and checked for any further corrections or the addition of more factors in the mitigation process. I also plan to work on it further using coherent fiber bundles (CFBs) and we plan to publish the follow-up paper to ([Roy 20]) and provide definitive guidance to the exoplanet community on the precision achievable in a range of sky brightness conditions.

List of Figures

1.1	Cosmic Milestone: NASA Confirms 5,000 Exoplanets (Image credits: nasa.gov)	2
1.2	Exoplanet Types Infographic (Image credits: nasa.gov)	3
1.3	Exoplanet Detection by Transit Method (Image credits: nasa.gov)	5
1.4	NASA’s Webb Takes Its First-Ever Direct Image of Distant World (Image credits: nasa.gov)	6
1.5	Demonstration of the principles of microlensing (Image credits: nasa.gov)	7
2.1	Radial velocity method of exoplanet detection(Image credits: nasa.gov)	9
2.2	Radial velocity method (Image credits: nasa.gov)	11
3.1	Example of the scattered lunar light (Image credits: [Yoachim 16])	14
3.2	NEID high-resolution (HR) mode port adapter fiber head that collects light from the telescope for transportation to the spectrometer. Left: image of the as-built fiber head being installed with NEID; Middle: diagram showing the relative placement of the coherent fiber bundles (CFBs) around the science fiber, as well as the position of the sky fiber. Right: Magnified CFB image from the manufacturer.	18
4.1	Cross Correlation Function. The order-by-order CCFs are summed, and the sum is fit by a Gaussian to measure a single RV value for the observation. (Image credits: NEID DRP)	22
4.2	Overview of the direct sky fiber cross-correlation CCF subtraction technique. Note that the spectrum and CCF continuum levels are matched for illustrative purposes only; in reality, the sky fiber has a much lower flux level. (Image credits: [Roy 20])	23
4.3	Overview of the model sky subtraction technique. Note that the spectrum and CCF continuum levels are matched for illustrative purposes only; in reality, the sky fiber has a much lower flux level. (Image credits: [Roy 20])	25
4.4	Test Pipeline	27

5.1	Overplots for scaled-down solar spectrum and sky ccf for TIC325554331 aka Barnard's star(Spectrum observed during bright sky)	32
5.2	Overplots for scaled-down solar spectrum and sky ccf for TIC325554331 aka Barnard's star(Spectrum observed during dark sky)	33
5.3	Overplots for scaled-down solar spectrum and sky ccf for HD9407 (Spec- trum observed during bright sky)	34
5.4	Overplots for scaled-down solar spectrum and sky ccf for HD9407 (Spec- trum observed during dark sky)	35
5.5	Overview of the simultaneous broadband correction technique. Note that the spectrum and CCF continuum levels are matched for illustrative pur- poses only; in reality, the sky fiber has a much lower flux level. (Image credits: [Roy 20])	38

List of Tables

5.1	Table showing radial velocity calculations for TIC325554331 for bright sky observations	30
5.2	Table showing radial velocity calculations for TIC325554331 for dark sky observations	31
A.1	Radial velocity signals for different kind of planets around solar-mass stars; ([Lovis 10])	41

Contents

Abstract	VII
List of Figures	IX
List of Tables	XI
1 Introduction	1
1.1 Exoplanets	1
1.1.1 History	1
1.1.2 Definition	2
1.1.3 Types	3
1.2 Detection Techniques	4
1.2.1 Radial Velocity	4
1.2.2 Transit Spectroscopy	4
1.2.3 Direct Imaging	5
1.2.4 Gravitational Microlensing	6
1.2.5 Astrometry	6
2 Radial Velocity Method	9
2.1 Introduction	9
2.2 Measuring Radial Velocities	10
2.2.1 Barycentric Motion	10
2.2.2 Precise Radial Velocities	11
2.2.3 Radial Velocity Jitter: Spurious Doppler Signals	12
3 Solar Contamination	13
3.1 Types of Light	14
3.1.1 Zodiacal Light	14
3.1.2 Scattered Moonlight	14
3.1.3 Airglow	15

3.1.4	Scattered Starlight	15
3.1.5	Atmospheric Emission Lines	15
3.1.6	Twilight	16
3.2	Effect of Solar Contamination on RV Measurements	16
3.3	NEID	18
3.3.1	NEID Data Reduction Pipeline (DRP)	19
4	Methodology	21
4.1	Cross-Correlation Function(CCF)	21
4.2	Correcting for Solar Contamination:	22
4.3	Using Sky Fiber/Direct Sky Fiber CCF Subtraction	22
4.3.1	Theory of Method	22
4.3.2	Usage of the Method	23
4.4	Using Theoretical Sky Contamination/ Model Sky Subtraction	24
4.4.1	Theory of Method	24
4.4.2	Brightness Tool	25
4.4.3	Correcting the Brightness Tool	26
4.4.4	Usage of the Method	26
5	Results & Discussions	29
5.1	Results	29
5.1.1	Comparison of Scaled Solar CCF with the sky fiber data of a few targets	29
5.1.2	Corrected Radial Velocity	30
5.2	Discussions	36
5.2.1	Limitations of the Sky Fiber	36
5.2.2	Simultaneous Broadband Correction using CFBs	37
6	Summary	39
A	Radial Velocity of Planets around Sun-like Stars	41

Chapter 1

Introduction

1.1 Exoplanets

1.1.1 History

Humans have long speculated whether there are other Earth-like planets and advanced civilizations there by gazing up at the stars. Although it has long been known that our solar system contains planets in addition to Earth, no one on Earth knew for a very long time whether the stars they saw in the night sky had any planets. Yet, we now have the technological means to discover planets orbiting other stars for the first time in human history. The discovery of exoplanets has led to a revolution in astronomy and astrophysics that has been underway for the past 30 years. In essence, an "exoplanet" is any planet that is located outside of our solar system. The discovery of exoplanets has created a whole new paradigm for astronomical investigation. One of humanity's most fundamental questions is "Are we alone in the universe?" The finding of exoplanets may provide an answer to this query. In addition to this fundamental one, there are other intriguing questions such as how many different kinds of exoplanets are there. Are planets that are like Earth common in the universe or in our galaxy? How do these planets form? What elements are present in their atmospheres? Which planet types can develop around binary stars? the list is endless. Only in the past 30 years have we really started on our adventure to discover other, far-off worlds through exoplanet exploration. The first planetary mass body outside of our solar system was discovered in 1992 ([Wolszczan 92]) near a pulsar. This was followed by the first unequivocal finding of an exoplanet, 51 Pegasi b, around a main sequence star in 1995 ([Mayor 95]). Exoplanet research became more prevalent as a result of this finding, which sparked numerous further discoveries in the years that followed.



Figure 1.1: Cosmic Milestone: NASA Confirms 5,000 Exoplanets (Image credits: nasa.gov)

1.1.2 Definition

Due to difficulties in the definition of a planet, especially at the extremities, such as for Jupiter size or larger planets, the International Astronomical Union (IAU) 2003 extra-solar planet working group recommended a definition ([Perryman 14]). The star-planet mass ratio has been added to the definition of ‘exoplanet’ as a result of discussion within the IAU Commission F2 “Exoplanets and the Solar System,” necessitating the hierarchical structure observed in our Solar System for an object to be referred to as an exoplanet. Additionally, if they meet the mass ratio condition, objects with planetary mass orbiting brown dwarfs are now regarded as exoplanets. As a result, the following is the IAU Commission F2 Exoplanets and the Solar System’s definition of an exoplanet as of August 2018.

“Objects with true masses below the limiting mass for thermonuclear fusion of deuterium (currently calculated to be 13 Jupiter masses for objects of solar metallicity) that orbit stars, brown dwarfs or stellar remnants and that have a mass ratio with the central object below the L_4 / L_5 instability ($M/M_{central} < 2 / (25 + \sqrt{621}) \approx 1/25$) are ‘planets’, no matter how they formed. The minimum mass/size required for an extrasolar object to be considered a planet should be the same as that used in our Solar System, which is a mass sufficient both for self-gravity to overcome rigid body forces and for clearing the neighborhood around the object’s orbit.”

The astonishing total of exoplanets discovered as of April 29, 2023, stands at 5338, and that figure is rising almost daily. The Kepler spacecraft has enabled the majority of these detections ([Borucki 11]). After the launch of the Transiting Exoplanet Survey Satellite (TESS) mission, this figure has also significantly increased ([Ricker 14]). With the James Webb Space Telescope, an ambitious scientific project that builds on the legacy of earlier space-based telescopes to push the boundaries of human knowledge even further in order

to address the questions of life beyond our solar system, it is anticipated that numbers will increase even more remarkably.

1.1.3 Types

Depending on its composition, each form of planet has a different internal and outer appearance.

1. **Gas giants** are planets that are similar in size or even far larger than Jupiter or Saturn, the largest planets in our solar system. Within these broad groups is much diversity. For instance, hot Jupiters, which are gas giants that orbit their stars so closely that their temperatures surge into the millions of degrees, were among the first planet kinds to be discovered (Fahrenheit or Celsius).
2. The size of **Neptunian planets** is comparable to that of Uranus or Neptune in our solar system. Although their internal compositions are expected to vary, all of them will have rocky cores and outer atmospheres that are dominated by hydrogen and helium.
3. Typically, terrestrial planets with or without atmospheres are referred to as **super-Earths**. They are lighter than Neptune yet have a mass greater than Earth.
4. **Terrestrial planets** are smaller than Earth and made of carbon, silicate, water, or rock. It will be discovered through further research whether some of them have atmospheres, oceans, or other evidence of habitability.

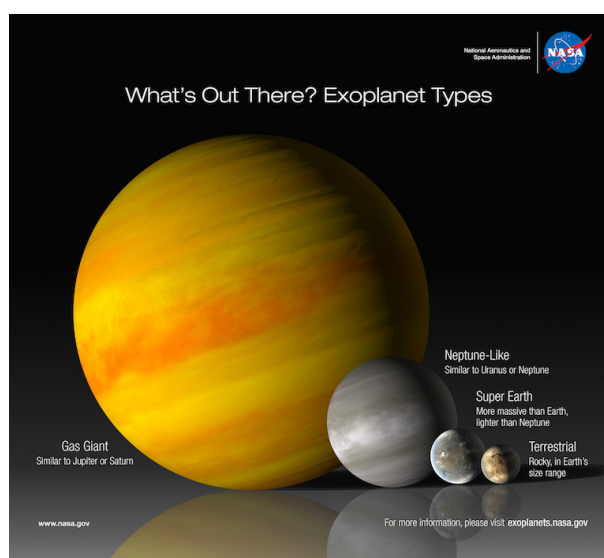


Figure 1.2: Exoplanet Types Infographic (Image credits: nasa.gov)

1.2 Detection Techniques

1.2.1 Radial Velocity

A hot, star-hugging gas giant planet that was identified in 1995 was thought to be roughly half the size of Jupiter. Its four-day orbit caused it to pull on its parent star so ferociously that, once astronomers learned what to look for, observatories on earth could see the star's wobble. This swift giant, also known as 51 Pegasi b, was discovered at the beginning of what is sometimes referred to as the "classical" period of planet discovery. One planet after another was discovered using the early method of tracking moving stars, many of which were massive "hot Jupiters" with tense, irradiating orbits.

The "radial velocity" of a star is measured using the wobbling technique. As a star moves a little bit closer to us and then a little bit farther away from us, the wavelengths of starlight are alternately compressed and stretched. These gyrations are brought on by gravitational forces from planets in orbit.

1.2.2 Transit Spectroscopy

Planet hunting entered what may be referred to as the "modern" era thanks to Kepler (2009–2018). Kepler positioned itself in an orbit that followed the Earth and then focused on a narrow region of the sky. It spent four years gazing at that region.

There were 150,000 stars in that modest region. Kepler was watching for minute drops in the brightness of individual stars brought on by planets passing in front of them. "Transit technique" is what it is termed. Once a planet has been discovered, its orbital size may be determined using the star's mass and period, which measure how long it takes the planet to complete one orbit. The same method is used by NASA's Transiting Exoplanet Survey Satellite, which was launched in 2018, to study large areas of our sky. Exoplanets have been found and additional details about them have been revealed, from planetary weather maps to components in atmospheres to mass characterizations, thanks to the usage of space telescopes like Spitzer and Hubble.

As our eyes in space get more acute, it allows us to examine the atmospheres of very far-off planets. The light collected by the telescopes can be analysed to determine the makeup of the atmospheres of exoplanets. Consider a prism: when white light is shone through it, it separates into a rainbow of colours. The colour bands of this spectrum can be scanned by scientists like a bar code to identify the substances that are present.

As light from a star passes through the atmosphere of an orbiting planet and eventu-

ally arrives at our telescopes, either in space or on the ground, it is a process known as “transit spectroscopy”, which provides information about where the light has been. Using spectroscopy, the Hubble Space Telescope has found helium and water vapour in planetary atmospheres. After its launch in 2021, the James Webb Space Telescope should provide more thorough profiles of exoplanet atmospheres.

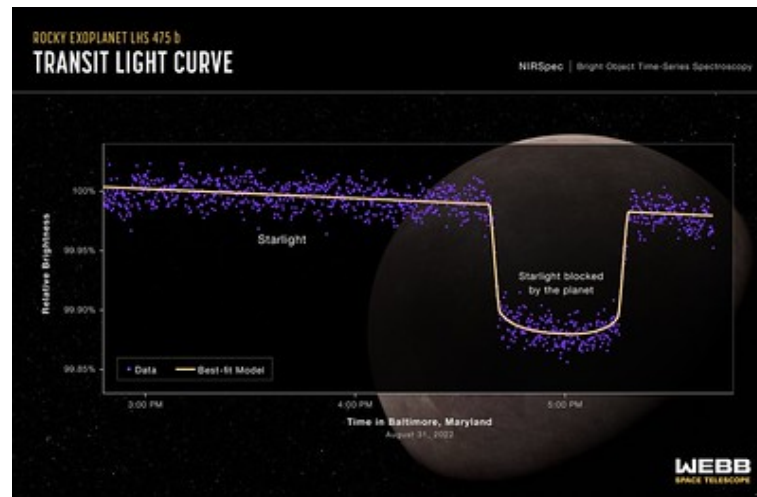


Figure 1.3: Exoplanet Detection by Transit Method (Image credits: nasa.gov)

1.2.3 Direct Imaging

To discern surface features, a single pixel of light directly acquired from an exoplanet will not be sufficient. The next best thing, however, will be provided by exoplanet atmospheric profiles and maybe by signs of gases indicating the presence of life. In the past, huge planets that are still so hot from their recent birth, that they are still self-luminous, have mostly been the subject of such “direct photographs” of exoplanets. One of the most remarkable is a movie made by astronomers using data from Hawaii’s Keck Observatory, which shows four exoplanets orbiting the star HR 8799. The **coronagraph** and the **starshade**, two technologies that are now undergoing rapid development, would be used by the next generation of space telescopes to look for direct photographs of exoplanets.

The coronagraph is designed to reduce the intense starlight so that the planets circling the stars can be seen. And it all happens inside the telescope, where a network of masks, prisms, and detectors work together to block out brightness. The telescope has self-flexing mirrors that flex in real time as it collects light that has travelled tens of light years from an exoplanet thanks to thousands of small, piston-like actuators. These “deformable mirrors” reduce starlight and improve the clarity of the planet’s light by making up for minor defects in telescope optics.

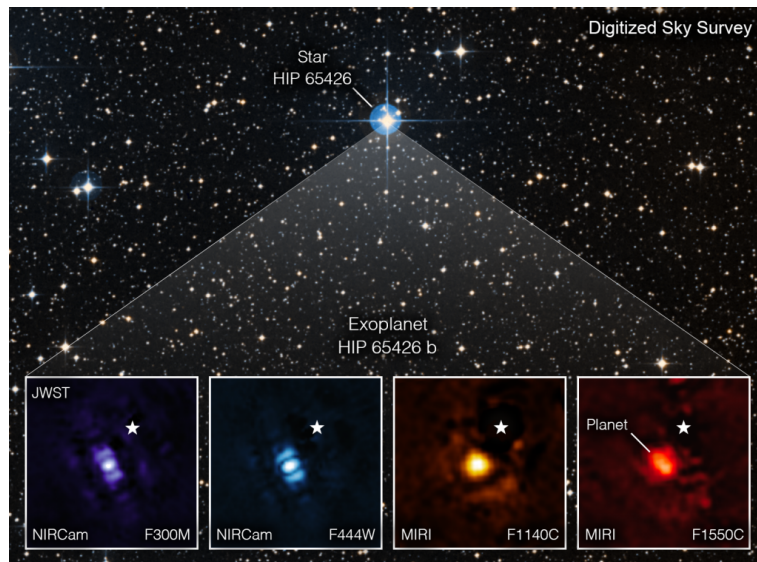


Figure 1.4: NASA's Webb Takes Its First-Ever Direct Image of Distant World (Image credits: nasa.gov)

The starshade is a different method of snuffing out starlight. This baseball diamond-sized, sunflower-shaped spacecraft would unfurl like an origami piece. Its unusual shape would obscure starlight and dampen any stray light that could otherwise leak around the edges when parked far from a space telescope. The starshade concept is being improved by NASA scientists in order to be taken into consideration for a potential future mission.

1.2.4 Gravitational Microlensing

Another technique for finding planets makes use of a phenomenon that Einstein first theorised: the power of gravity to bend and twist starlight. The light from a background star that passes directly behind a star in the foreground will be amplified by the star's gravity. When a background star passes in front of the foreground star, the star will appear to a correctly placed telescope as a spike in light intensity; the planet will show as a second, smaller spike. This method, now utilised by ground telescopes, will be used by NASA's Nancy Grace Roman Space Telescope to find exoplanets.

1.2.5 Astrometry

Astrometry is used to look for the periodic wobble that a planet induces in the position of its parent star. The minimum detectable planet mass gets smaller in inverse proportion to the planet's distance from the star. From the ground, the Keck telescope is being equipped to measure angles as small as 20 micro-arc seconds, leading to a minimum detectable mass in a 1 AU orbit of $66M_{earth}$ for a solar-mass star at 10 pc.

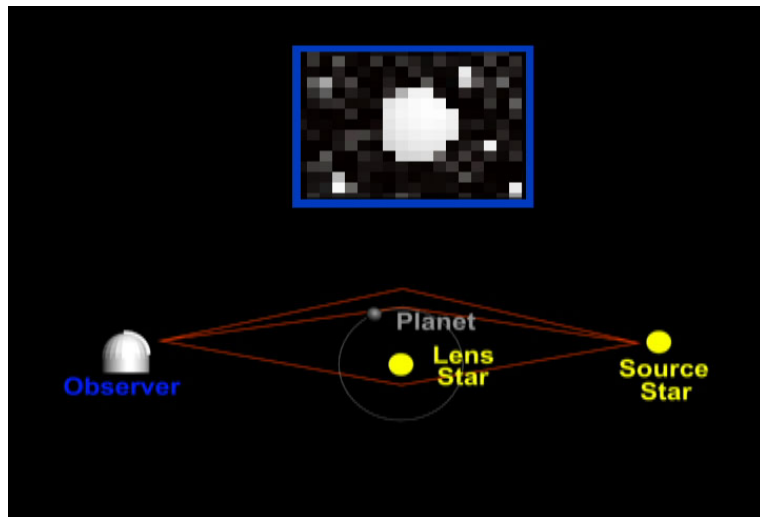


Figure 1.5: Demonstration of the principles of microlensing (Image credits: nasa.gov)

Chapter 2

Radial Velocity Method

2.1 Introduction

The majority of what we know about the skies comes from data that has been encoded in different types of light. Even though studies of meteorites, in situ measurements of the solar system by space probes, the detection of high energy particles, and more recently observations of astronomical neutrinos and gravitational waves have all contributed to many significant advances, the vast majority of astronomical observations are still made by extracting as much information from photons as possible.

Due to this limitation, some characteristics of stars and galaxies are considerably easier to ascertain than others. Although distances can frequently only be approximated, positions on the sky can be measured with extreme accuracy. The situation is typically flipped for the time derivatives of these numbers; whilst motions of objects in the plane of the sky may be undetectable due to the immense distances involved, radial velocities may frequently be determined with high accuracy. Since a large portion of astronomy is concerned with the

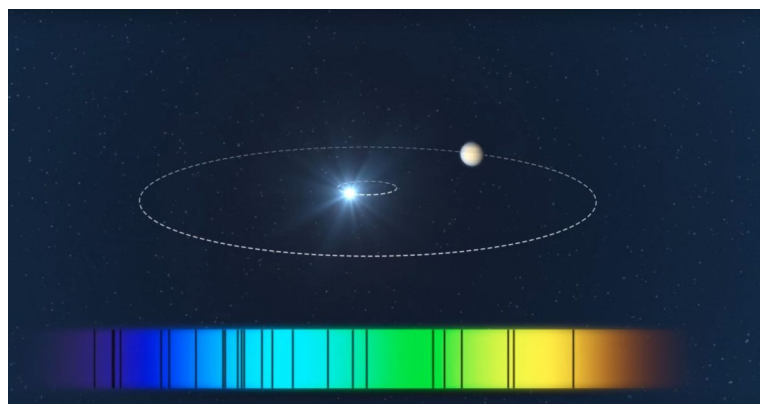


Figure 2.1: Radial velocity method of exoplanet detection(Image credits: nasa.gov)

motions of objects as a result of their mutual gravitation, radial velocity measurements are

naturally a key component of this field of study. They have shown the existence of invisible planets, dark matter, and the expansion and acceleration of the universe itself. They tell us the masses of everything from moons in the solar system to stars and galaxies.

2.2 Measuring Radial Velocities

When ions, atoms, and molecules in stellar atmospheres imprint numerous absorption lines on starlight, we are able to calculate or quantify the remaining wavelengths of these lines using atomic physics. These lines are Doppler shifted to their observed wavelengths by a star’s radial motion. The Doppler formula then allows astronomers to calculate the relative radial speed between the star and the observatory that measured the light, v_r via the redshift z :

$$z = \frac{\lambda_{obs} - \lambda_{rest}}{\lambda_{rest}} = \frac{1}{\gamma(1 + v_r/c)} - 1 \quad (2.1)$$

Here c is the speed of light and γ is the relativistic factor $1/(1 - (v/c)^2)$.

Absolute radial velocities, which are measurements of radial velocity made with reference to the “laboratory” in this way, are the cornerstones of our knowledge of the dynamics of the Galaxy and the expansion of the Universe. The accuracy of these observations is constrained by the spectrograph’s wavelength calibration and knowledge of complication factors such internal motions of the emitting material and redshifts resulting from general relativity. Absolute radial velocities of stars are often accurate to within 100 m/s ([Chubak 12]). Differential radial velocities, or the change in redshift between two epochs, can be used to obtain more accurate observations. Differential measurements have the advantage that certain uncertainties (like those resulting from systematic effects, imperfectly known rest wavelengths, or the model of the emitting material) will have an equal impact on all measurements made with a particular instrument or technique, and so differences between measurements are not adversely affected by them. As a result, measurements of the change in the absolute redshift of a star’s spectral characteristics can be made with more than two orders of magnitude higher precision.

2.2.1 Barycentric Motion

The barycentre is defined as the centre of mass for two or more bodies orbiting one another. In the context of the Solar System, the barycentre is its centre of mass. While observations are usually taken by observatories on Earth, it is important to correct them to ensure they reflect measurements taken in an inertial frame moving in tandem with the barycentre. This is necessary because the Earth itself rotates at a speed of 300 m/s and moves at a speed of 30 km/s around the Sun. Thus, any observatory on Earth trying to measure the radial velocity

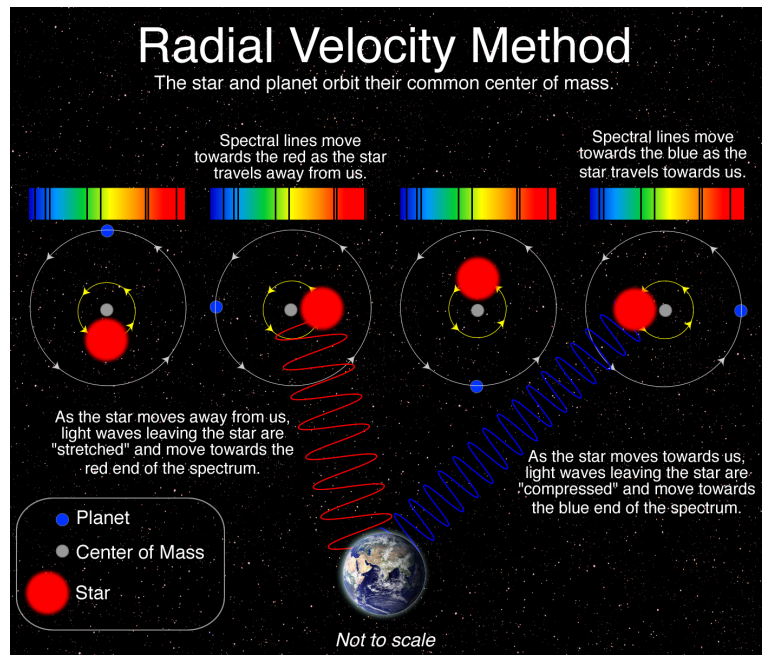


Figure 2.2: Radial velocity method (Image credits: nasa.gov)

of even a perfectly stable star would find variations over a diurnal or annual period because of this motion. Making a barycentric adjustment or correction accounts for this motion.

The motion of the barycentre is given by the barycentric velocity, which is frequently much greater than the motions of the stars in their orbits, and the barycentric correction for stars moving as a result of planets can be four or five orders of magnitude greater. So, practically speaking, the challenge of radial velocity precision is one of measuring modest redshifts extremely precisely, frequently to one part in 10^4 or better, rather than one of measuring very small redshifts.

Thankfully, the velocity of the Earth has been extensively investigated and quantified for tasks requiring far greater accuracy than exoplanet discovery. The Jet Propulsion Laboratory and others maintain ephemerides (tables describing the positions of celestial bodies as functions of time) for the Earth in the barycentric frame, allowing for highly accurate predictions of the orientation of the Earth into the future (and measurements of orientations are available, for example, through the International Earth Rotation Service). Lastly, all contemporary observatories offer accurate timekeeping, enabling later barycentric correction algorithms to tag observations with the proper time stamp.

2.2.2 Precise Radial Velocities

Absorption cell spectroscopy and spectrograph stabilisation are the two main techniques of precise radial velocimetry used to find and describe exoplanets via the reflex velocities of their host stars. They differ mostly in how the spectrograph is calibrated. The spec-

trograph’s wavelength calibration is the main factor limiting the accuracy of differential redshift measurements. A single pixel shift corresponds to a change in radial velocity of 1 km/s in typical RV spectrographs, which resolve starlight with a power of $R = \lambda / \Delta\lambda \sim 50,000\text{--}100,000$. As giant planets would alter the velocities of their host stars by orders of tens of m/s, this corresponds to a precision of 10^{-2} pixels, while for discovering Earth-mass planets it needs to be a few orders of magnitude better than that. As typical astronomical detector pixels are $15\ \mu\text{m}$ across, one is measuring star line “motions” to within a few nanometers.

Spectrographs used in astronomy are not this steady. The spectrograph can be used for a variety of purposes because the majority are multipurpose instruments with plenty of movable elements that are activated. From night to night, a given wavelength of light cannot usually be expected to land much closer to its normal position than a pixel (or year to year). The answer is to use a combination of differential method, calibration, and stabilisation. During the course of several nights, precise differential measurements were possible because of the stabilisation and calibration process. Since then, this method has been utilised to the fullest extent possible. Modern stable radial velocimeters employ cryostats and vacuum chambers to precisely regulate the vibration, temperature, and pressure of spectrographs. The remaining, inevitable changes in the spectrograph are monitored using emission sources like laser frequency combs, which are locked to atomic clocks and offer nearly perfect wavelength references. These changes can result from slow changes in the crystalline structure of the metals involved or irregular thermal outputs from the detector electronics.

2.2.3 Radial Velocity Jitter: Spurious Doppler Signals

The motions of gas in stellar atmospheres and across the differentially spinning star disc result in absorption, emission, scattering, and other phenomena that are observed in stellar spectroscopy. In addition to an actual center-of-mass movement of the star itself, the lines’ shape and centroid positions will change as a result of numerous other factors. This phenomenon, known as jitter, can occur throughout a range of timelines, amplitudes, and noise distributions. Spotty, quickly revolving, and low-gravity stars are most affected.

This not only presents the more pernicious problem of false detections around these stars, a problem that has dogged the field since its inception (e.g. [Queloz 01]), but also renders detection sensitivity progressively worse for younger and more developed stars. Many avoidance and mitigation strategies are needed to find a solution to the issue of finding planets with Doppler amplitudes close to or below the level of the jitter.

Chapter 3

Solar Contamination

The desire to find Earth-mass planets in the habitable zone has sparked an ongoing struggle for ever-higher accuracy measurements in the field of radial velocity (RV) exoplanet detection ([Kopparapu 13]). Doppler reflex signals of 10 cm s^{-1} are produced by such terrestrial-mass planets circling Sun-like stars, and this nominally determines the precision objective for several next-generation equipment and surveys. Formerly insignificant sources of error become prominent at these levels of scrutiny, necessitating significant advancements in both instrument design and analytical methods ([Fischer 16]). This is the domain of “extreme” precision spectroscopy. It is now necessary to conduct in-depth research on and take precautions against a number of previously unidentified events that impact spectral line profiles. Building ever-larger telescopes has been a current astronomical trend. Because telescope time is continuously in demand, careful planning of observations is required due to the high operational costs of very enormous telescopes. To understand how long an exposure is required for a given observation with a specific signal to noise ratio, more precise predictions and estimates of the sky background are therefore required. The predicted sky background from various sources is computed by the ESO model using basic principles.

In this part, I thoroughly explain the sky elements incorporated into the ESO model as well as the sampling strategy we used to produce multi-dimensional grids of model spectra. This ESO Model further forms the basis for the ‘Brightness Tool’ I used for sky background calculations.

3.1 Types of Light

3.1.1 Zodiacal Light

Zodiacal light, also known as the ecliptic or plane of the zodiac, is a band of light in the night sky that is believed to be sunlight reflected from cometary dust. In the tropics, where the ecliptic is roughly vertical, the light is plainly seen in the west after dusk and in the east before dawn. It is best visible at mid-northern latitudes in the morning in September and October and in the evening in February and March. At a position 30° from the Sun to roughly 90° on the ecliptic, the zodiacal light can be seen visually following it. According to photometric observations, the band extends to the area opposite the Sun, where a faint augmentation known as the gegenschein, or counter glow, is discernible. All portions of the sky include some zodiacal light, which is a continuation of the Sun's F-corona. The ESO model varies the zodiacal light as a function of ecliptic coordinates and airmass.

3.1.2 Scattered Moonlight

The scattered moonlight is the most prominent natural source of brightness in the night sky and is also the main cause of sky background noise. For accurate estimate of the sky background, a trustworthy moonlight model is essential. Also, a lot of observers are attempting to characterise faint objects by spectroscopy, and astronomers would be able to forecast which spectral features are observable within a specific exposure time if they had a precise understanding of the background spectrum. We boost the telescope scheduling efficiency by refining the dispersed moonlight model within a sky background model. Most

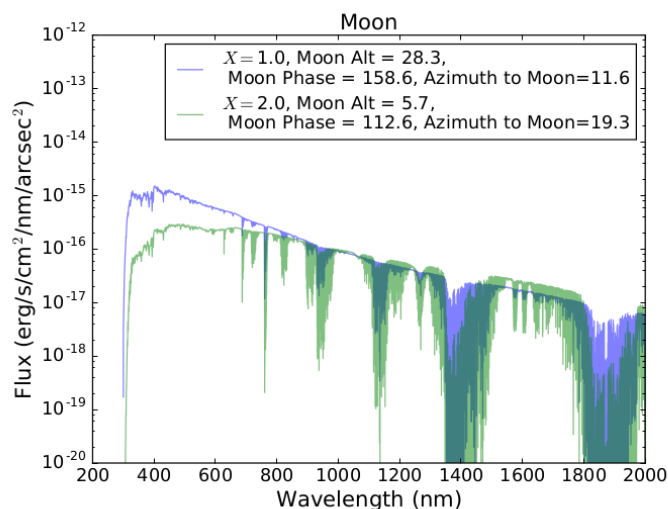


Figure 3.1: Example of the scattered lunar light (Image credits: [Yoachim 16])

of the sunlight that shines on the Moon’s surface and a small amount of earthlight are reflected back as moonlight. A template library of scattered moonlight is built in the ESO Model by considering Moon-Sun separations of 0° to 180° in 15° steps, and moon altitudes from 15° to 90° ; ([Yoachim 16]). Then the expected spectrum is computed on a grid of 29 positions across the sky. This is a HEALPix grid (with an n_{side} of 4, resolution of $\sim 15^\circ$), based on altitude and azimuth (relative to the moon), where pointings with an airmass greater than 2.6 are ignored. This results in a total of 2,262 template spectra for the scattered moonlight. Examples of the scattered moonlight spectra are shown in Figure 3.1.

3.1.3 Airglow

An atmospheric emission of light known as airglow, also called nightglow, occurs on planets. Even if the impacts of starlight and diffused sunlight from the far side are eliminated, the night sky on Earth never truly darkens due to this optical phenomenon. Self-illuminating gases are the source of this phenomenon, which is unrelated to either sunspot activity or the magnetism of the Earth.

The recombination of atoms that were photoionized by the Sun during the day, luminescence from cosmic rays striking the upper atmosphere, and chemiluminescence, which is primarily caused by oxygen and nitrogen reacting with hydroxyl free radicals at heights of a few hundred kilometres, are all processes that contribute to airglow. Because of the glare and light scattering during the day, it is not visible. A ground observer may be able to see airglow at night if it is light enough, and it typically has a bluish appearance.

The airglow is assumed to be a function of airmass and solar activity as measured by solar radio observations.

3.1.4 Scattered Starlight

The ESO model utilises a mean spectrum for the dispersed starlight because it makes up a relatively small portion of the sky background. This element only depends on airmass.

The gas molecules and dust in the interstellar medium absorb and scatter starlight, like all other types of electromagnetic (EM) radiation. The atomic and molecular makeup of the inter-stellar matter (ISM) affects these activities.

3.1.5 Atmospheric Emission Lines

Although the airglow and emission lines change during the night and with the seasons, the variance is just 10–20 %. “For scheduling observations, the variation in background caused by airmass and distance to the moon should swamp any effects from the skylines fading

during the night,” ([Yoachim 16]). The lower atmosphere is included for completeness even though it only emits in the IR. The ESO Model takes template spectra with airmasses ranging from 1 to 2 with steps of 0.1 and furthermore an airmass of 2.5 under the assumption that the atmospheric emission is solely a function of airmass. The upper atmosphere, lower atmosphere, and dispersed star light are unified into a single component in the calculations in the ESO Model code because they only differ as a function of airmass.

3.1.6 Twilight

The ESO sky model does not include a component for sunlight scattered by earth’s atmosphere. The twilight sky brightness is difficult to compute from first principles. While scattered moonlight can be computed via a single or double scattering model, the solar twilight comes from multiple scatterings, thus there is no simple analytic model for computing the solar twilight from first principles and models must instead rely on Monte Carlo radiative transfer simulations.

Rather than computing radiative transfer, ESO Model advises fitting a simple empirical model to the twilight flux. Data from the all-sky camera as well as other sites show that after the Sun’s altitude drops below $\sim -10^\circ$, the twilight flux decays exponentially with solar altitude. The total sky brightness is well fit by an exponential decay plus a zeropoint offset.

3.2 Effect of Solar Contamination on RV Measurements

Due to the large reduction in our capacity to measure intrinsic stellar line profiles caused by spectral pollution, spectral contamination is still a major problem for calculating RV error estimates ([Pepe 08]). The worst example of contamination is when spectral patterns in the superimposed light are present. These features can both contaminate specific line forms and cause an erroneous velocity signal to be generated across the ensemble of lines. This is made worse by the fact that the movement of the star and the Earth-based observatory over time frequently introduces relative shifts between the contaminant and source spectra. For seeing-limited equipment, there are no hardware alternatives to completely minimise the effect of background sky brightness on RV observations. In reality, it is frequently necessary to determine the contaminant’s amount from the same observations that must be adjusted for the effect. It is theoretically possible to counteract this, but it is impractical given competition from other subfields like extragalactic and cosmological investigations. Blended light from partners or unfavourable backdrop objects have been known to provide misleading false positives, necessitating careful handling (e.g., [Wright 13]). We concen-

trate on scattered or reflected sunlight, which is practically always present in observed spectra from ground-based detectors at some degree, as opposed to the incidental character of these contaminants. The degree of this contamination is affected by a number of variables, such as the brightness of the sky, target-moon separation, lunar phase, ecliptic latitude, zenith angle, and solar cycle phase ([Krisciunas 97]). This error source has largely been mitigated by avoiding the following observations so far: (1) those made in the twilight; (2) those made during a full moon or when the target is close to the moon; and (3) those made in cloudy skies or cirrus clouds ([Pepe 08]; [Seager 10]).

For the modern equipment operating in the ≥ 1 m/s accuracy zone, ensuring that the sky backdrop is faint (>7 – 10 magnitudes fainter as a general rule of thumb) has mainly been sufficient ([Pepe 08]). The possibility of doing solar contamination correction for Doppler measurements at the 10 cm s^{-1} level has not yet been reached. In weighted mask-based ([Pepe 02]) or high signal-to-noise ratio (S/N) template-based cross-correlation for radial velocity measurement, the presence of scattered sunlight in observed spectra can be a two-fold source of error, affecting both “peak pulling” and the introduction of more complex and time-variable structure in the cross-correlation function (CCF) or χ^2 space.

([Roy 20]) carefully evaluated how solar light contamination may affect RV measurements and investigated how a simultaneous sky fibre can help. A dedicated sky fibre is included in a number of new instruments, such as NEID ([Schwab 16]) and KPF ([Gibson 18]), for the correction of telluric absorption and emission lines and the elimination of scattered sunlight. Even when there is a direct impact on RV precision, the sky fibre in these systems is highly spectrally scattered, making it challenging to evaluate even very low levels of solar pollution.

[Roy 20] investigated the feasibility of replacing the sky fibre with broadband sky images from coherent fibre bundles for scenarios of very faint sky with low S/N in the sky fibre (CFBs). CFBs are primarily employed in the NEID fibre head for target acquisition, but they also offer an intriguing alternate channel for measurements of the brightness of the sky. Efforts were made to keep the simulations applicable to next-generation spectrographs with limited viewing. Parameters were based, where specification was required, on the NEID spectrograph, which was installed on the 3.5m WIYN telescope at Kitt Peak. These calculations can therefore be easily modified for use with other instruments by making adjustments for the telescope aperture, the size and form of the fibre, the instrument’s bandpass and resolution, and the anticipated sky conditions.

3.3 NEID

NEID (NN-EXPLORE Exoplanet Investigations with Doppler Spectroscopy) is an optical EPRV (Extreme Precision Radial Velocity) Spectrograph on the WIYN 3.5-meter Telescope at Kitt Peak National Observatory, Arizona, USA. The name NEID is derived from the word meaning “to see” in the native language of the Tohono O’odham, on whose land Kitt Peak National Observatory is located. The NEID fiber head comprises sky fiber, science fiber, cal fiber, and coherent fiber bundles (CFBs). The wavelength coverage for NEID is 380-930 nm (continuous coverage). Resolution for NEID is $\sim 110,000$ in “High Resolution” mode and $\sim 70,000$ in “High Efficiency” mode. NEID uses a dedicated sky fiber to directly sample the solar contamination spectrum at a resolution identical to the target spectrum unlike other spectrographs like HARPS.

The NEID fiber head comprises sky fiber, science fiber, cal fiber, and coherent fiber bundles (CFBs). The science fiber focuses on the target star while the sky fiber focuses on the sky region around the target star. CFBs also look at the sky region but are on a different detector. These fibers are expected to reliably correct for the scattered sunlight noise. The solar contamination spectrum is directly sampled by instruments like NEID at a resolution that is the same as the target spectrum using a specialised sky fibre. The science and sky fibres should have comparable levels of sky flux because they are of the same size and are separated by only a modest distance ($22''$ on-sky in the case of NEID, Figure 3.2).

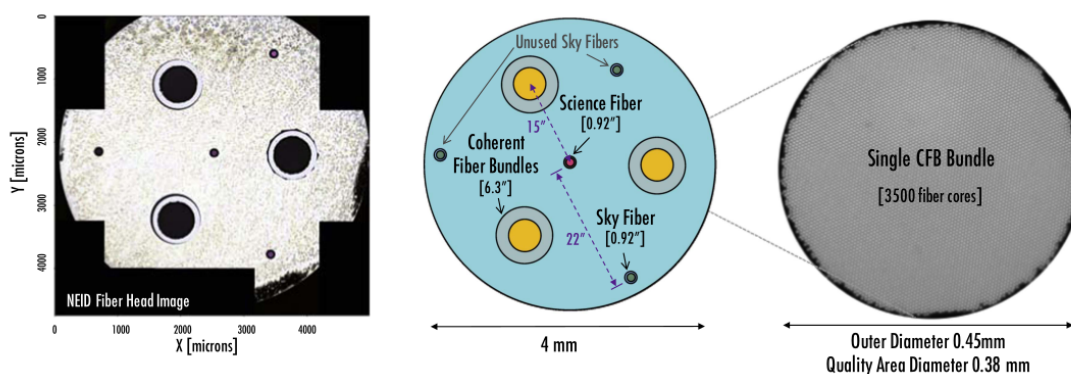


Figure 3.2: NEID high-resolution (HR) mode port adapter fiber head that collects light from the telescope for transportation to the spectrometer. Left: image of the as-built fiber head being installed with NEID; Middle: diagram showing the relative placement of the coherent fiber bundles (CFBs) around the science fiber, as well as the position of the sky fiber. Right: Magnified CFB image from the manufacturer.

3.3.1 NEID Data Reduction Pipeline (DRP)

Source: NEID-DRP 1.2.0 documentation

The NEID Data Reduction Pipeline (NEID-DRP) processes data obtained with the NEID Precision Radial Velocity Spectrometer at 3.5 m WIYN Observatory on Kitt Peak.

Three levels of data products are generated:

- Level 0: Raw data produced by the NEID instrument control system at the WIYN observatory.
- Level 1: Extracted, wavelength calibrated spectra.
- Level 2: Derived products, including radial velocities, activity indicators, and telluric models.

NEID GTO (Guaranteed Time Observations) data is obtained at night by professional observers operating the spectrometer in a Queue based mode. During daytime hours, from 9:30 to 15:30 MST, the spectrograph uses its solar telescope feed to automatically obtain a continuous stream of solar spectra, with a cadence of 55 s/exposure, followed by ~ 30 s of readout.

Calibration data is primarily obtained in two large blocks each day from 16:00 - 18:30 MST, and from 6:30 - 9:00 MST. Data transfers automatically from Kitt Peak to NExScI twice per day, following completion of these calibration sequences. After arrival at NExScI, validation checks are performed to ensure data integrity, and the data is ingested into the NExScI archive.

Chapter 4

Methodology

4.1 Cross-Correlation Function(CCF)

The cross correlation function between two different signals is defined as the measure of similarity or coherence between one signal and the time delayed version of another signal. Cross-correlation functions (CCFs) yield the measurements of radial velocity (RV). The extracted wavelength-calibrated spectra produced in level 1 files are used to calculate the radial velocity (RV) of each observation. RVs are derived by cross correlating target spectra with a weighted numerical stellar mask based on spectral type ([Baranne 96], [Pepe 02]). The NEID pipeline currently uses the public release of the ESPRESSO masks. While mask lines are historically selected empirically for RV stability, the mask width is set by the resolution of the instrument to cover approximately 1 pixel (in the case of NEID, this translates to 1 km/s).

The module operates on each echelle order to produce individual cross-correlation functions (CCFs) that are stored in extension 12 of the level 2 files. These are fit with Gaussians to produce order-by-order RV measurements that can be used to scrutinize chromatic behaviors. The order-by-order CCFs are then summed, and the sum is fit by a Gaussian to measure a single RV value for the observation. This aggregate value is stored in the level 2 header, along with the corresponding measured uncertainty, and the BJD_TDB.

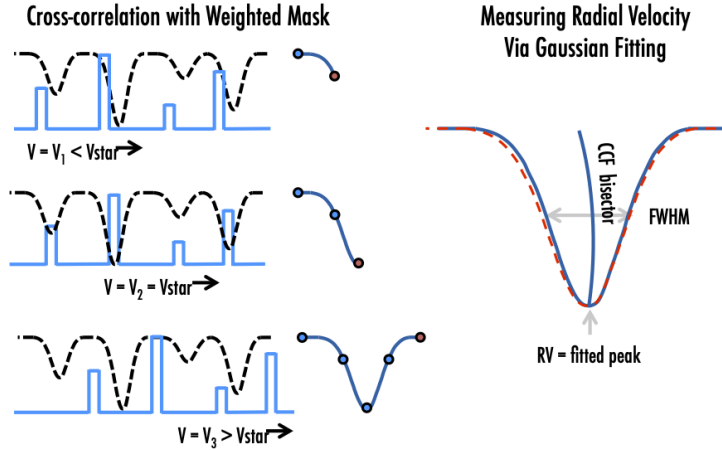


Figure 4.1: Cross Correlation Function. The order-by-order CCFs are summed, and the sum is fit by a Gaussian to measure a single RV value for the observation. (Image credits: NEID DRP)

4.2 Correcting for Solar Contamination:

The usage of the sky fibre and other auxiliary data must be optimised across the observing circumstances of the telescope location, therefore solar contamination correction will need to be a crucial algorithmic component of next-generation RV pipelines. Now I discuss that the extent of adjustment that may be made, and inherent drawbacks to account for this effect in the coming sections via two methods.

4.3 Using Sky Fiber/Direct Sky Fiber CCF Subtraction

4.3.1 Theory of Method

Sky correction has already been tried in the realm of precise RV measurements by directly subtracting the CCF of the scientific fibre spectrum from the CCF of the sky fibre spectrum. Figure 4.2 depicts this method's overview. Direct CCF subtraction is a straightforward yet effective method that makes use of the inclusion of a sky fibre with the same fibre size and cross section as the science fibre (and hence a very similar line spread function). In a real instrument, the two fibres may have slightly differing throughputs and aberrations, which makes a relative scaling between the CCFs necessary before subtraction. Although it was primarily intended as a coarse correction of strong moonlight contamination to save some observations, this method has been successfully applied to the SOPHIE spectrograph ([Barge 08]; [Hébrard 08]; [Pollacco 08]; [Bonomo 10]; [Santerne 11a], [Santerne 11b]).

[Bonomo 10] also points out that the CCF bisectors, a technique frequently employed to identify spectral contamination ([Wright 13]) or stellar activity problems ([Robertson 14]) in RV observations, quickly show peak tugging from moonlight contamination. By dividing the science fibre CCF by the sky fibre CCF in simulated scenarios ([Roy 20]), this correction approach can be tested. This significantly lessens the contamination effect, reducing the worst RV errors from ~ 100 m/s to ~ 10 cm/s. This residual inaccuracy is caused by noise in the removed sky fibre CCF as well as a change in the mean velocity recorded after CCF subtraction (residual peak tugging from sky) and an increase in the standard deviation of the measured noise distribution.

Sky fiber CCFs become dominated by read noise as the sky gets darker, and do not actually correct for it. The fact that contamination mistakes are already minimal when the sky is dark, however, masks this effect. Even after performing 1000 realisations for each combination of star and sky, anomalies in the contours still exist because these minor changes are challenging to measure, even on simulated spectra.

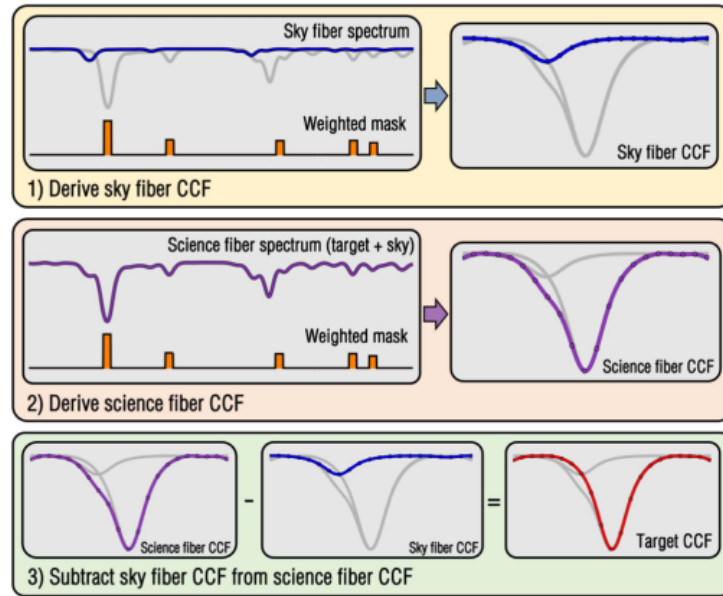


Figure 4.2: Overview of the direct sky fiber cross-correlation CCF subtraction technique. Note that the spectrum and CCF continuum levels are matched for illustrative purposes only; in reality, the sky fiber has a much lower flux level. (Image credits: [Roy 20])

4.3.2 Usage of the Method

For direct sky subtraction method:

- I chose four targets, ie HD9407, HD127334, HD185144, TIC325554331 for my project mainly because these had the most abundant data out of all the stars observed

using NEID.

- The NEID Data Reduction Pipeline (DRP) by default calculates CCF for the science fiber. I modified the pipeline to calculate CCF for the sky fiber data.
- I ran the CCF function on the sky fiber data of the above mentioned four targets.
- Ideally as predicted before commissioning of the instrument, the CCF on the sky fiber should have shown a scattered light contamination signal, but we didn't observe the signal due to high noise in the sky fiber data.
- Hence directly subtracting the sky fiber CCF from the science fiber CCF was not going to be helpful. This led me to explore the other methods.

4.4 Using Theoretical Sky Contamination/ Model Sky Subtraction

4.4.1 Theory of Method

A different approach to removing contamination entails subtracting a noiseless (or extremely high S/N) model sky spectrum from the science fibre spectrum using the flux captured in the sky fibre as the basis (see Figure 4.3). The absolute brightness of the sky is directly correlated with the continuous level of the sky fibre CCF:

$$SkyBrightness = 2.5 \times \log\left(\frac{constant}{CCF\ continuum}\right) \quad (4.1)$$

With this technique, we may quantify the continuum level and RV position of the dispersed sunlight with relation to the target star by fitting the sky fibre CCF with a gaussian. Since the sky spectrum is roughly travelling at the barycentric velocity, the CCF centre can either be set or subject to strict constraints during peak fitting. A noiseless model sky spectrum is scaled to the appropriate flux level using the anticipated sky brightness. The same synthetic spectrum that was utilised to create the injected sky spectrum is employed in this idealised scenario. For improved line-spread function (LSF) matching, this model should really be derived from a library of high-S/N observations of the local twilight sky, preferably made through the science fibre itself.

The model sky spectrum is subtracted from the science fibre spectrum to provide a final CCF of the corrected target spectrum. This method also significantly lowers the solar contamination impact, resulting in the worst RV errors dropping from ~ 100 m/s to ~ 1 m/s. However, it does not perform as well as a straightforward subtraction of the sky fibre CCF because the extra processes of measurement, translation, and spectrum interpolation can

result in minute errors.

In situations where direct CCF subtraction is inappropriate, such as when the sky and

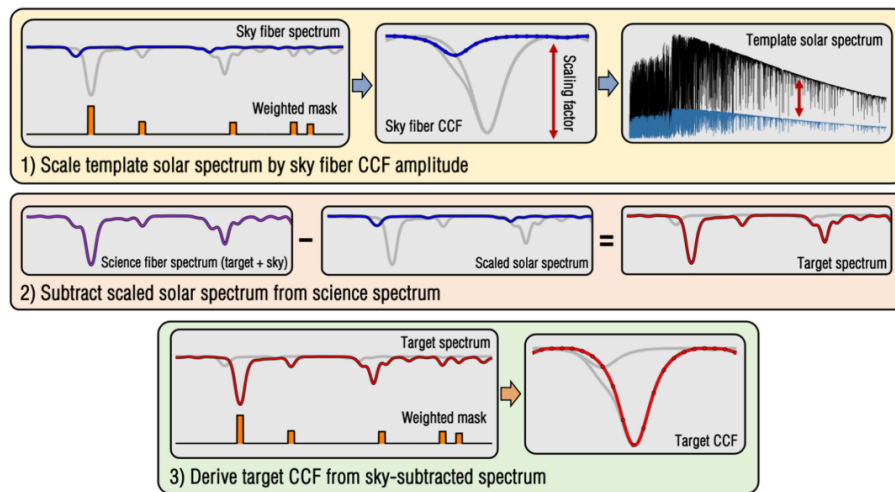


Figure 4.3: Overview of the model sky subtraction technique. Note that the spectrum and CCF continuum levels are matched for illustrative purposes only; in reality, the sky fiber has a much lower flux level. (Image credits: [Roy 20])

science fibres have different geometries or spectral resolutions, this technique may be especially helpful. In low-sky background levels where it is challenging to distinguish the continuum, using the sky spectrum CCF to scale the template solar spectrum may be more advantageous than using the recorded sky spectrum directly. To make sure that the model spectrum matches the genuine sky spectrum based on site, airmass, moon phase, and other observable variables, there is an additional load.

4.4.2 Brightness Tool

We call the sky brightness code as ‘Brightness Tool’ developed by Arvind Gupta (Penn State University) that computes flux from sky coordinates and time stamps.

- It takes input as input-time, input-ra (right ascension), inputdec (declination), input-loc (location), equinox='J2000'.
- It calculates and returns the twilight and scattered moonlight contributions to sky brightness in magnitudes / (arcsec)² and the corresponding radial velocity precision in cm/s.
- It has various functions like:
 - calc_moon()** which calculates the moonlight contribution to sky brightness.
 - calc_twilight()** which calculates the twilight contribution to sky brightness.

calc_positions() which calculates the various parameters like moon phase angle, moon zenith angle, target zenith angle, target-moon distance , target-Sun azimuth, target airmass and solar altitude.

sky_brightness() which finally gives us the sky brightness contributed by twilight and moonlight and radial velocity precision.

4.4.3 Correcting the Brightness Tool

We encountered a bug in the brightness tool such that the moon position in the function was inconsistent from our independent calculations. The bug was that the moon angle was calculated with respect to the moon, Sun and the star. But we wanted to calculate the moon angle with respect to the moon, observatory and the star. Hence I fixed this bug and corrected the brightness tool to be used for calculations.

4.4.4 Usage of the Method

I build a test pipeline which involved the following steps.

- When direct sky fiber CCF calculation didn't help us in observing a scattered solar light contamination signal, I tried the theoretical calculation method.
- I read both a solar file data and a target star sky fiber data observed during NEID.
- I used the brightness tool (after debugging it) by modifying it further according to my requirements to calculate the total sky brightness for different target stars.
- I used the total sky brightness and also the exposure time for that particular sky brightness value calculated as inputs to my function called **calc_snr()**. I made this function calculate the expected signal to noise ratio for a given target for particular temperature, wavelength, v-magnitude of star and the exposure time. It also calculates the signal to noise ratio for the solar file data. It returns the expected snr for the target star at given conditions and the ratio between the expected snr and the calculated snr.
- I used **ccf_retrieve()** to take input as ccf of the solar data and the ratio between the science and sky fiber data. This function then scales down the solar file ccf using this ratio value and return the scaled down solar ccf, which is thus my theoretical prediction of the solar light contamination in the sky fiber data for a particular target for particular mask.
- I also incorporated functions from the prv/CCF (a private repository for NEID) to fit the gaussian to the ccf to calculate the mean of the radial velocity.

- I subtracted the modelled solar ccf from the science fiber data and got the corrected ccf and derived radial velocity from it
- I then called all these functions by just giving the target star data as input and the pipeline I built automatically did all the calculations and gave me as results:
 - 1) The overplots of expected solar light contamination containing scaled-down solar ccf and the sky fiber data ccf.
 - 2) RV (radial velocity) before the correction.
 - 3) Radial velocity after the correction.
- I also ran CCF code on science fiber of solar file convolved with not just G2 but M2 and K2 espresso masks as well.

In this way, I developed a test pipeline code to predict expected sky contamination, for a given star with a mask of choice, from a solar spectrum convolved with a given mask. Thus, I also got the difference my pipeline is making in radial velocity calculations by correction using sky fiber data for particular category of stars.

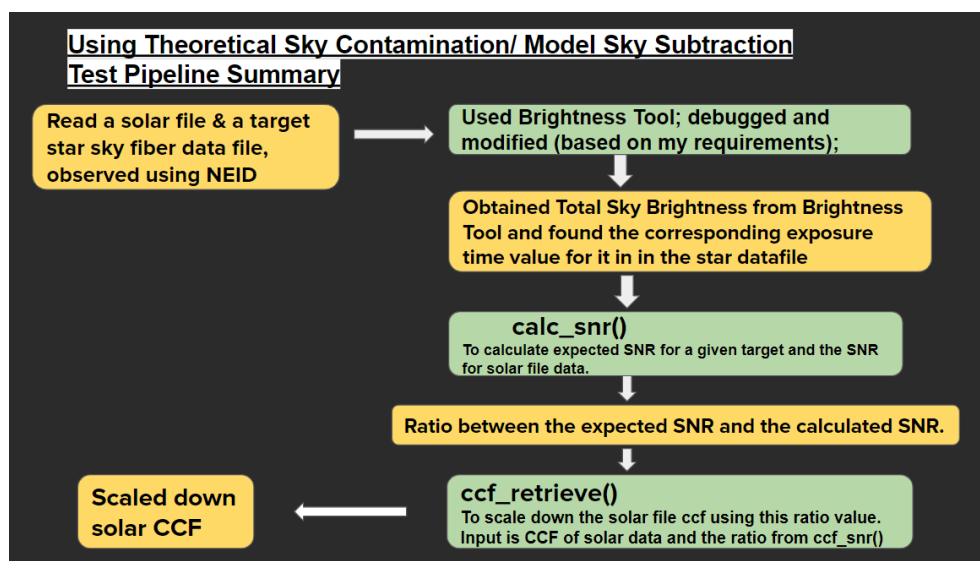


Figure 4.4: Test Pipeline

Chapter 5

Results & Discussions

5.1 Results

The work during this project helps to conclude the following points:

5.1.1 Comparison of Scaled Solar CCF with the sky fiber data of a few targets

- Obtained the cross-correlation function (CCF) of the scattered light in the sky fiber of NEID data.
- As explained in depth in the Methodology section, I built up a pipeline to theoretically calculate the solar light contamination for a given star with a given mask.
- This pipeline also helped me compare the model ccf with the fiber data ccf.
- For m-dwarfs (i.e., Barnard's star/TIC325554331), a scattered solar light signal was observed, which matched our theoretical prediction of solar contamination signal using G2 mask convolved solar spectrum, but it was higher by a scaling factor of around 5.
- In the exact same conditions as mentioned in the last point, for spectrum observed during dark sky, no signal was seen, thus confirming that sky fiber is working.
- For solar type stars, even on a dark sky, when no contamination signal was expected, we could still see a signal as shown in the plots attached, especially Figure 5.4
- For solar type stars (like HD9407), the signal we obtained from sky fiber was orders of magnitude stronger than what we expected. This was found to be fiber to fiber scattered light contamination.

Note: Here in the attached figures, I have shown the overplots of the scaled solar ccf and the sky fiber data ccf for different target stars. The mask I used in CCF calculations is G2.espresso (the one used for sun-like stars) irrespective of the star types. It is for visualization purposes to see the maximum level of solar contamination signal. But for calculation of corrected ccf and RV, I use the right mask corresponding to the target star, ie, G2 mask for G2 stars and M2 mask for m-dwarfs, etc.

5.1.2 Corrected Radial Velocity

After obtaining the predicted values of sky contamination and the modelled ccf, I was also able to obtain:

- The corrected CCF after subtraction of the uncorrected science ccf and modelled sky ccf.
- Radial velocity of the science fiber data, i.e., radial velocity for the uncorrected CCF.
- Radial velocity of the corrected CCF.
- The difference in the radial velocity for a particular mask for a star with a particular spectral type.

Here I have tabulated the RV(before and after correction) calculated for an m-dwarf, ie, Barnard’s star during the bright and dark sky observations. Note: For subtraction of CCFs, I used the same mask as that of the star type for CCF calculation; here I used M2.espresso mask for m-dwarf (TIC325554331/Barnard’s star).

RV (km/s) (uncorrected)	RV (km/s) (corrected)	RV difference (cm/s)
0.12	0.12	-9.06
0.12	0.12	-28.74
0.12	0.12	-11.59
0.12	0.12	-8.46
0.11	0.11	-17.80

Table 5.1: Table showing radial velocity calculations for TIC325554331 for bright sky observations

RV (km/s) (uncorrected)	RV (km/s) (corrected)	RV difference (cm/s)
0.12	0.12	-4.73e-10
0.12	0.12	-9.35e-10
0.12	0.12	-4.64e-9
0.09	0.09	-2.31e-8
0.12	0.12	-6.60e-9

Table 5.2: Table showing radial velocity calculations for TIC325554331 for dark sky observations

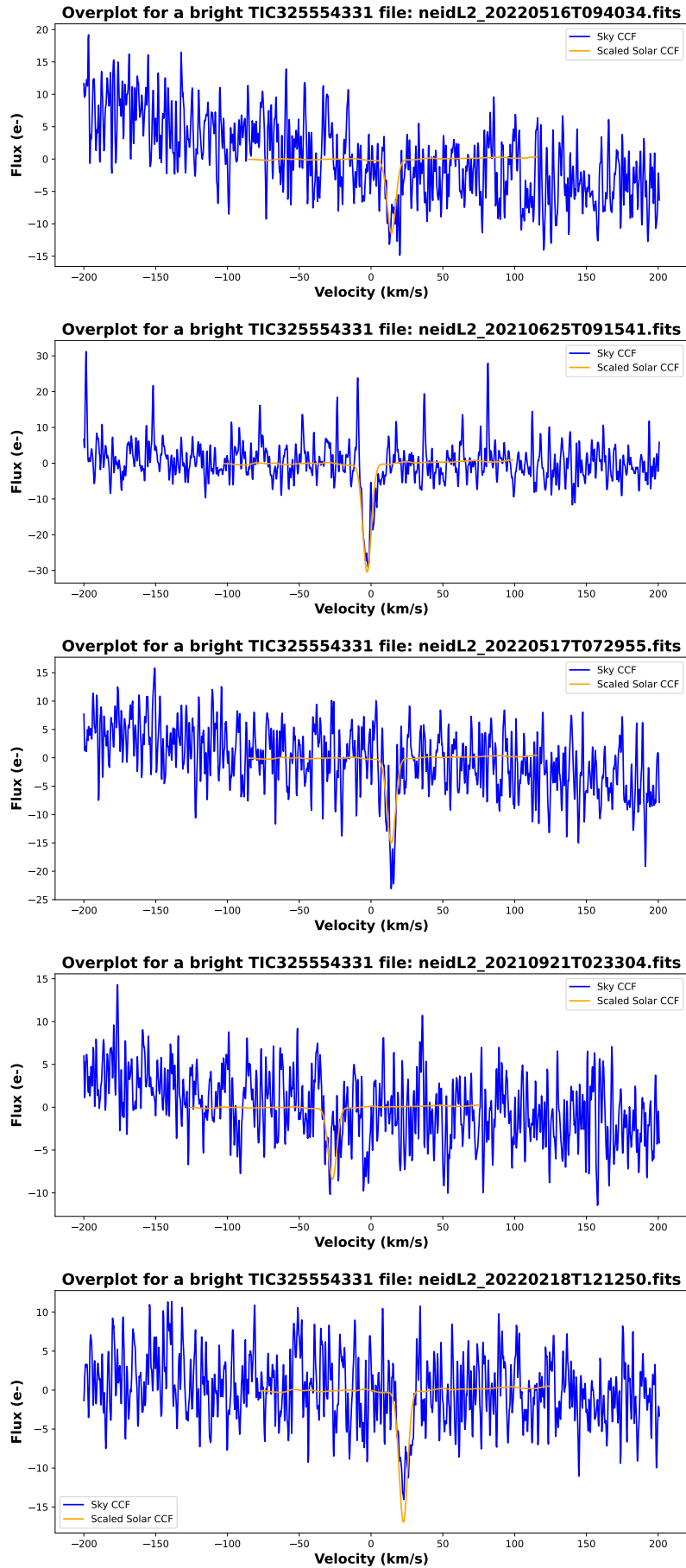


Figure 5.1: Overplots for scaled-down solar spectrum and sky ccf for TIC325554331 aka Barnard's star (Spectrum observed during bright sky)

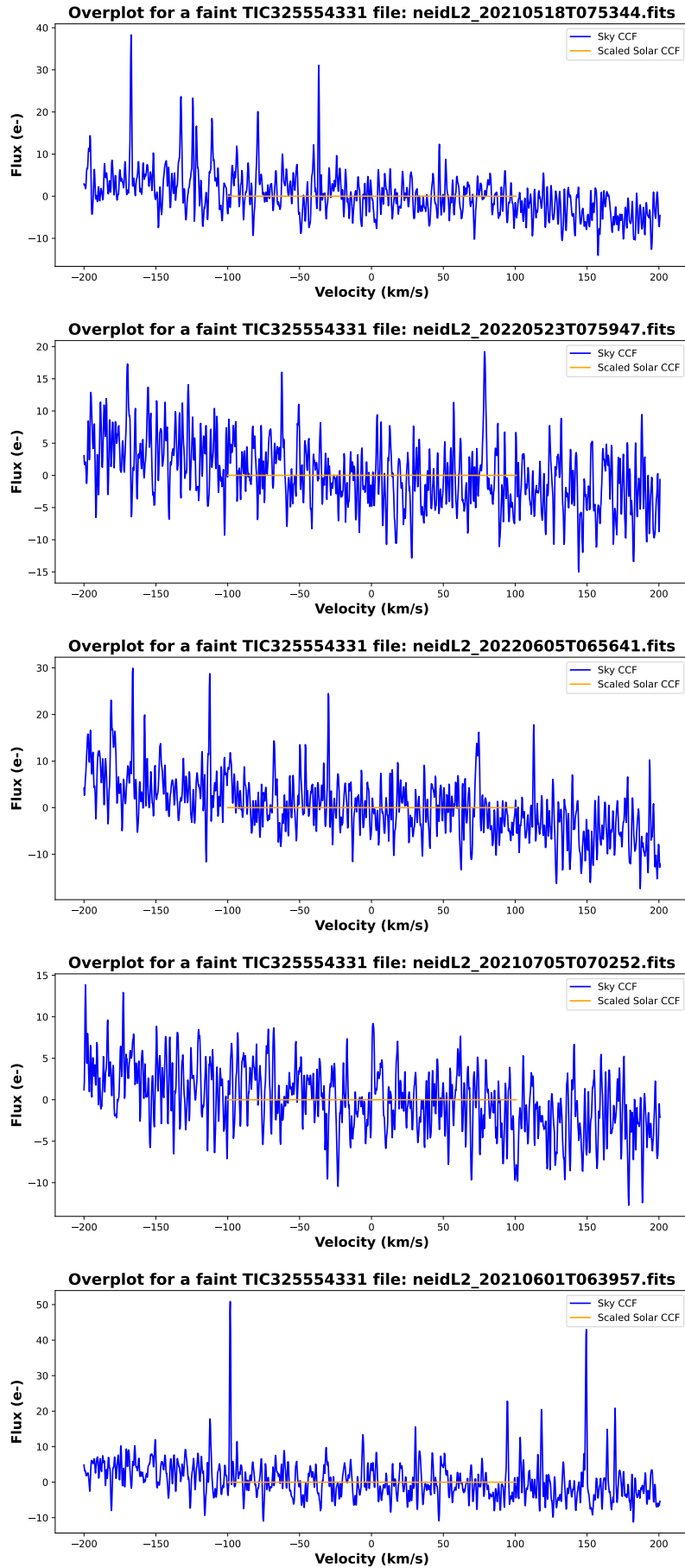


Figure 5.2: Overplots for scaled-down solar spectrum and sky ccf for TIC325554331 aka Barnard's star (Spectrum observed during dark sky)

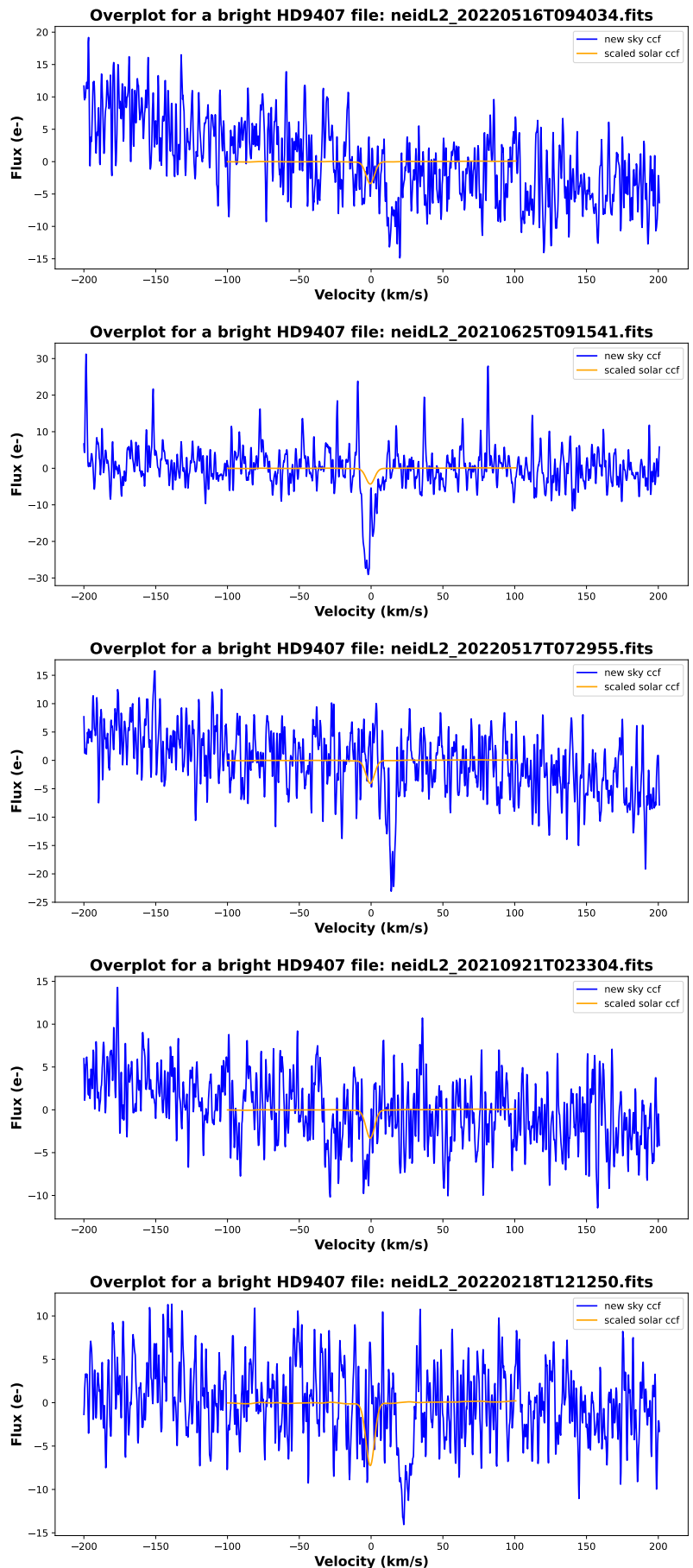


Figure 5.3: Overplots for scaled-down solar spectrum and sky ccf for HD9407 (Spectrum observed during bright sky)

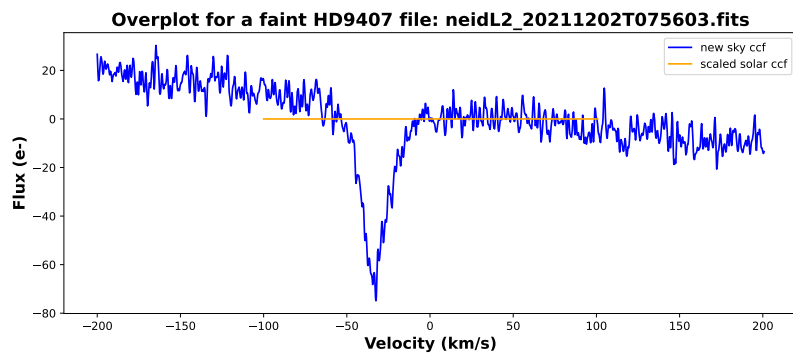
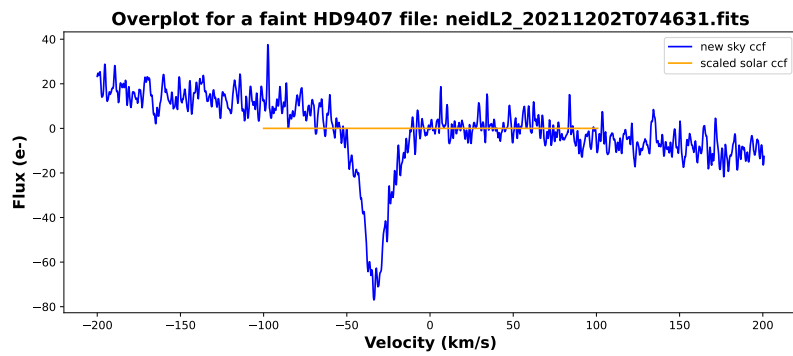
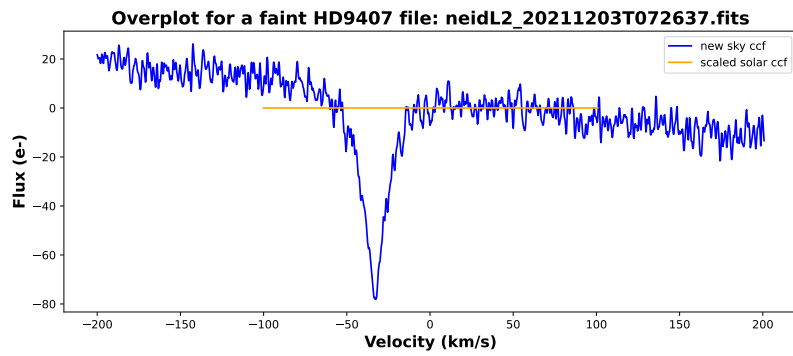
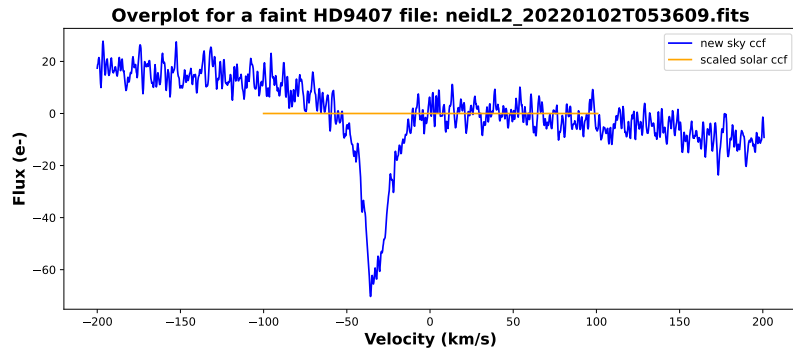
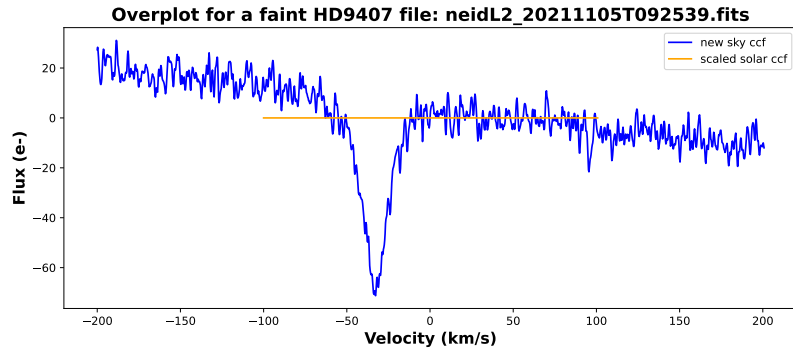


Figure 5.4: Overplots for scaled-down solar spectrum and sky ccf for HD9407 (Spectrum observed during dark sky)

5.2 Discussions

1. In the results, we saw that for solar-type stars, the signal we obtained from sky fiber was orders of magnitude stronger than what we expected. Detailed analysis showed that scattered starlight in the science fiber is overwhelming the signal in the sky fiber ccf if the spectral type of the star is close to the Sun. This was found to be fiber-to-fiber scattered light contamination. It shows that there are some limitations of the sky fiber, and we need to come up with a better technique or method to mitigate the issue.
2. Thus, the pipeline I developed works well, as confirmed by the m-dwarf dataset. Now I need to design a method to predict the sky fiber contamination in solar-like stars using the sky fiber data in M type star observations as well as work this out using the coherent fiber bundles (CFB) data. The reason for using CFBs is that they are called as proxy sky fibers because they also focus on the sky around the target star. But CFBs are located on a different detector, hence fiber-to-fiber scattered light contamination could be avoided which seems to have affected our sky fiber data.

Therefore I will further subtract the sky fiber CCF from the science fiber CCF for the masks with the right spectral types, thus correcting for the contamination. Hence aiming to mitigate the deleterious effects of solar contamination on RV precision. Thus the work intends to aid in identifying terrestrial planets in the habitable zones (HZs) of other stars. And here I discuss the details of the two points highlighted above:

5.2.1 Limitations of the Sky Fiber

The usage of a simultaneous sky fibre is a prerequisite for both of the sun contamination correction methods discussed in the Methodolgy section. The CCF subtraction technique also depends on the similarity between the science and sky fibers (or the ability to transform the LSF and chromatic variability between the two). There may be instances, though, where a sky fibre is either not accessible (in some devices, one must choose between calibration light and sky lighting in the contemporaneous fibre) or the sky fibre itself has contamination problems. The sky fibre is contaminated mostly at two different points.

1. The first occurrence takes place at the port adapter fibre head (Figure 3.2) and is brought on by the stellar PSF's wings spreading into the sky fibre's coverage region ($22''$ separation). The sky fibre receives an extra 0.001 percent of contaminated flux for a $V_{mag}=12$ star at a sky brightness of $17 \text{ mag } (\text{arcsec})^{-2}$; when the sky dims to $21.45 \text{ mag } \text{arcsec}^{-2}$ (typical for WIYN dark time at zenith), this rises to 0.08 percent. Given the intention to sample the same (or a neighbouring) region of sky,

contamination at the port fibre head is inevitable regardless of the device. Better seeing naturally lessens the impact of this effect, but the fact that it changes depending on the observing environment complicates modelling efforts.

2. Cross-contamination between fibre traces on the detector, which is brought on by low-level wings of the cross-dispersion profile, is the second and more serious cause for concern. The leakage of starlight from the same echelle order into the sky fibre (intraorder contamination), which is predicted to occur at 10^{-3} to 10^{-5} levels, is not particularly troublesome in the CCF correction approach because it effectively yields a primary CCF peak that is somewhat diminished. However, the function of star brightness has a significant impact on attempts to measure sky brightness from the sky fibre. Interorder contamination increases significantly at the red end of the NEID bandpass as the distance between the sky fibre and the next-door calibration order decreases to about ~ 7 pixels (as opposed to about ~ 80 pixels at the blue end). The light from the calibration source (laser frequency comb, etalon, or emission lamp) quickly overpowers any attempts to measure the spectrum of the sky fibre.

5.2.2 Simultaneous Broadband Correction using CFBs

Simultaneous broadband measurements can offer significant redundancy and may end up being the only practical choice for the darkest skies due to the low flux levels and worries about contamination in the sky fibre. This technique samples the background sky using broadband imaging, preferably quite close to the target object, to determine the amount of dispersed solar irradiance. By doing this, a solar contamination estimate is produced that is independent of the high-resolution sky spectrum, which may be noisy. Figure 5.5 depicts the method in broad strokes. Many astronomical observatories use CFBs for target acquisition, guiding, and maintaining focus because they are flexible image guides with large fields of view compared to typical spectrograph fibres ([Ramsey 03]; [Newman 04]; [Smee 13]; [Yan 16]). Three CFBs are placed around the science fibre in the port adapter fibre head for NEID.

Figure 3.2 displays an enlarged view of a single CFB as well as the relative positioning of the CFBs in relation to the science and sky fibres in NEID. The CFBs collect a significant amount of sky light concurrently with science observations. Bright stars floating into their frames of view are given additional redundancy by the existence of three bundles. The CFBs are a crucial addition to the sky fibre since they are resistant to worries of cross-contamination on the detector, despite the fact that contamination from stellar light at the port adapter fibre head can also damage them ($15''$ separation from science fibre).

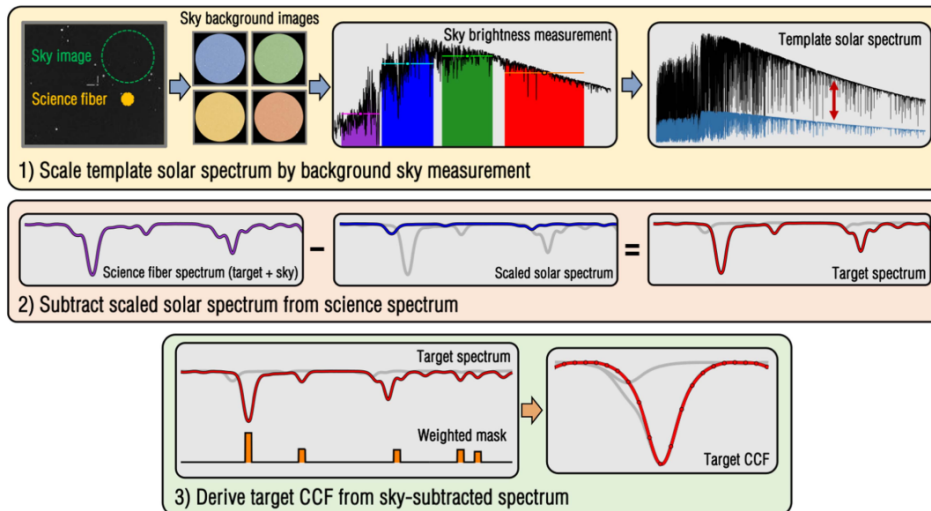


Figure 5.5: Overview of the simultaneous broadband correction technique. Note that the spectrum and CCF continuum levels are matched for illustrative purposes only; in reality, the sky fiber has a much lower flux level. (Image credits: [Roy 20])

The CFBs offer a fresh and effective method for correcting solar contaminant via concurrent broadband sky imaging. A scaling link can be established between the CCF continuum and the absolute sky brightness in the V-band by examining CFB images in conjunction with the science fibre observing the comparatively bright sky. Thus, the sky brightness level observed from the CFB can be utilised to create a noiseless model sky spectrum and subtract it from the science spectrum.

Chapter 6

Summary

Solar light contamination from lunar and atmospheric scattering of sunlight, results in systematic errors in stellar radial velocity (RV) measurements. It can significantly reduce the 10 cm s^{-1} sensitivity required to detect and characterize terrestrial exoplanets in or near habitable zones of Sun-like stars ([Roy 20]). NEID is an optical extreme precision radial velocity spectrograph on the WIYN 3.5-meter Telescope at Kitt Peak National Observatory, Arizona, USA. The NEID fiber head comprises sky fiber, science fiber, cal fiber, and coherent fiber bundles (CFBs). The science fiber focuses on the target star while the sky fiber focused on the sky region around the target star. CFBs also look at the sky region but are on a different detector. These fibers are expected to reliably correct for the scattered sunlight noise.

CCFs yield the measurements of radial velocity (RV). RVs are derived by cross-correlating target spectra with a weighted numerical stellar mask based on spectral type. The order-by-order CCFs are then summed, and the sum is fit by a Gaussian to measure a single RV value for the observation. The CCF of the sky fiber is computed by cross-correlation with a numerical mask. Sky fiber CCF is subtracted from the CCF of the science fiber spectrum. The final target RV is derived from the resultant corrected target CCF.

Using a brightness tool, I calculated sky contamination for more abundant target data. Following [Roy 20], I modified the pipeline configuration to get CCF for sky fiber. Plots are attached in the Results section. I ran CCF code on science fiber of solar file convolved with not just G2 but M2 and K2 espresso masks as well. I made a test pipeline code to predict expected sky contamination for a given star with a mask of choice, from a solar spectrum convolved with a given mask.

So I obtained the CCF of the scattered light in the sky fiber of NEID data. For solar type stars, the signal we obtained from sky fiber was orders of magnitude stronger than what we expected. This was found to be fiber to fiber scattered light contamination. For m-dwarfs, a scattered solar light signal was observed, which matched our theoretical prediction of so-

lar contamination signal using G2 mask convolved solar spectrum, but it was higher by a scaling factor of around 5. In the exact same conditions, for spectrum observed during dark sky, no signal was seen, thus confirming that sky fiber is working.

Detailed analysis shows that scattered starlight in the science fiber is overwhelming the signal in the sky fiber ccf if the spectral type of the star is close to the Sun. Thus I need to design a method to predict the sky fiber contamination in solar like stars using the sky fiber data in M type star observations. I also plan to explore the CFBs which haven't been worked upon yet, as they are expected to not have the fiber-to-fiber scattered light contamination like the sky fibers. Thus the pipeline is working well and I am able to obtain the corrected radial velocity. I need to further subtract the sky fiber CCF from the science fiber CCF for the masks with the right spectral types for all observed targets as well, thus correcting for the contamination. Hence I aim to mitigate the deleterious effects of solar contamination on RV precision. Thus the work intends to aid in identifying terrestrial planets in the habitable zones (HZs) of other stars.

Appendix A

Radial Velocity of Planets around Sun-like Stars

This table lists a few typical examples for planets with different masses and semi-major axes orbiting a solar-mass star. As one can see, the search for exoplanets with the RV technique requires a precision of at least ~ 30 m/s to detect giant planets. Towards lower masses, a precision of ~ 1 m/s is necessary to access the domain of Neptune-like planets and super-Earths, while measurements at ~ 0.1 m/s would be able to reveal the Earth. ([Lovis 10])

Planet	a (AU)	K_1 (m/s)
Jupiter	0.1	89.8
Jupiter	1.0	28.4
Jupiter	5.0	12.7
Neptune	0.1	4.8
Neptune	1.0	1.5
Super-Earth ($5 M_{\oplus}$)	0.1	1.4
Super-Earth ($5 M_{\oplus}$)	1.0	0.45
Earth	0.1	0.28
Earth	1.0	0.09

Table A.1: Radial velocity signals for different kind of planets around solar-mass stars; ([Lovis 10])

Bibliography

- [Baranne 96] A. Baranne, D. Queloz, M. Mayor, G. Adrianzyk, G. Knispel, D. Kohler, D. Lacroix, J. P. Meunier, G. Rimbaud & A. Vin. *ELODIE: A spectrograph for accurate radial velocity measurements.* , vol. 119, pages 373–390, October 1996.
- [Barge 08] P. Barge, A. Baglin, M. Auvergne, H. Rauer, A. Léger, J. Schneider, F. Pont, S. Aigrain, J. M. Almenara, R. Alonso, M. Barbieri, P. Bordé, F. Bouchy, H. J. Deeg, De La Reza, M. Deleuil, R. Dvorak, A. Erikson, M. Fridlund, M. Gillon, P. Gondoin, T. Guillot, A. Hatzes, G. Hebrard, L. Jorda, P. Kabath, H. Lammer, A. Llebaria, B. Loeillet, P. Magain, T. Mazeh, C. Moutou, M. Ollivier, M. Pätzold, D. Queloz, D. Rouan, A. Shporer & G. Wuchterl. *Transiting exoplanets from the CoRoT space mission. I. CoRoT-Exo-1b: a low-density short-period planet around a G0V star.* , vol. 482, no. 3, pages L17–L20, May 2008.
- [Bonomo 10] A. S. Bonomo, A. Santerne, R. Alonso, J. C. Gazzano, M. Havel, S. Aigrain, M. Auvergne, A. Baglin, M. Barbieri, P. Barge, W. Benz, P. Bordé, F. Bouchy, H. Bruntt, J. Cabrera, A. Collier Cameron, L. Carone, S. Carpano, Sz. Csizmadia, M. Deleuil, H. J. Deeg, R. Dvorak, A. Erikson, S. Ferraz-Mello, M. Fridlund, D. Gandolfi, M. Gillon, E. Guenther, T. Guillot, A. Hatzes, G. Hébrard, L. Jorda, H. Lammer, A. F. Lanza, A. Léger, A. Llebaria, M. Mayor, T. Mazeh, C. Moutou, M. Ollivier, M. Pätzold, F. Pepe, D. Queloz, H. Rauer, D. Rouan, B. Samuel, J. Schneider, B. Tingley, S. Udry & G. Wuchterl. *Transiting exoplanets from the CoRoT space mission. X. CoRoT-10b: a giant planet in a 13.24 day eccentric orbit.* , vol. 520, page A65, September 2010.
- [Borucki 11] William J. Borucki, David G. Koch, Gibor Basri, Natalie Batalha, Timothy M. Brown, Stephen T. Bryson, Douglas Caldwell, Jørgen Christensen-Dalsgaard, William D. Cochran, Edna DeVore, Edward W. Dunham, III Gaugier Thomas N., John C. Geary, Ronald Gilliland, Alan Gould, Steve B.

Howell, Jon M. Jenkins, David W. Latham, Jack J. Lissauer, Geoffrey W. Marcy, Jason Rowe, Dimitar Sasselov, Alan Boss, David Charbonneau, David Ciardi, Laurance Doyle, Andrea K. Dupree, Eric B. Ford, Jonathan Fortney, Matthew J. Holman, Sara Seager, Jason H. Steffen, Jill Tarter, William F. Welsh, Christopher Allen, Lars A. Buchhave, Jessie L. Christiansen, Bruce D. Clarke, Santanu Das, Jean-Michel Désert, Michael Endl, Daniel Fabrycky, Francois Fressin, Michael Haas, Elliott Horch, Andrew Howard, Howard Isaacson, Hans Kjeldsen, Jeffery Kolodziejczak, Craig Kulesa, Jie Li, Philip W. Lucas, Pavel Machalek, Donald McCarthy, Phillip MacQueen, Søren Meibom, Thibaut Miquel, Andrej Prsa, Samuel N. Quinn, Elisa V. Quintana, Darin Ragozzine, William Sherry, Avi Shporer, Peter Tenenbaum, Guillermo Torres, Joseph D. Twicken, Jeffrey Van Cleve, Lucianne Walkowicz, Fred C. Witteborn & Martin Still. *Characteristics of Planetary Candidates Observed by Kepler. II. Analysis of the First Four Months of Data.* , vol. 736, no. 1, page 19, July 2011.

[Chubak 12] C. Chubak, G. Marcy, D. A. Fischer, A. W. Howard, H. Isaacson, J. A. Johnson & J. T. Wright. *Precise Radial Velocities of 2046 Nearby FGKM Stars and 131 Standards.* arXiv e-prints, page arXiv:1207.6212, July 2012.

[Fischer 16] Debra A. Fischer, Guillem Anglada-Escude, Pamela Arriagada, Roman V. Baluev, Jacob L. Bean, Francois Bouchy, Lars A. Buchhave, Thorsten Carroll, Abhijit Chakraborty, Justin R. Crepp, Rebekah I. Dawson, Scott A. Diddams, Xavier Dumusque, Jason D. Eastman, Michael Endl, Pedro Figueira, Eric B. Ford, Daniel Foreman-Mackey, Paul Fournier, Gabor Fű rész, B. Scott Gaudi, Philip C. Gregory, Frank Grundahl, Artie P. Hatzes, Guillaume Hébrard, Enrique Herrero, David W. Hogg, Andrew W. Howard, John A. Johnson, Paul Jorden, Colby A. Jurgenson, David W. Latham, Greg Laughlin, Thomas J. Loredo, Christophe Lovis, Suvrath Mahadevan, Tyler M. McCracken, Francesco Pepe, Mario Perez, David F. Phillips, Peter P. Plavchan, Lisa Prato, Andreas Quirrenbach, Ansgar Reiners, Paul Robertson, Nuno C. Santos, David Sawyer, Damien Segransan, Alessandro Sozzetti, Tilo Steinmetz, Andrew Szentgyorgyi, Stéphane Udry, Jeff A. Valenti, Sharon X. Wang, Robert A. Wittenmyer & Jason T. Wright. *State of the Field: Extreme Precision Radial Velocities.* Publications of the Astronomical Society of the Pacific, vol. 128, no. 964, page 066001, may 2016.

[Gibson 18] Steven R. Gibson, Andrew W. Howard, Arpita Roy, Christopher Smith, Sam Halverson, Jerry Edelman, Marc Kassis, Edward H. Wishnow, Michael

Raffanti, Steve Allen, Jason Chin, David Coutts, David Cowley, Jim Curtis, William Deich, Tobias Feger, Daniel Finstad, Yulia Gurevich, Yuzo Ishikawa, Ean James, Elisha Jhoti, Kyle Lanclos, Scott Lilley, Tim Miller, Steve Milner, Tom Payne, Kodi Rider, Constance Rockosi, Dale Sandford, Christian Schwab, Andreas Seifahrt, Martin M. Sirk, Roger Smith, Julian Stuermer, Marie Weisfeiler, Mavourneen Wilcox, Adam Vandenberg & Peter Wizinowich. *Keck Planet Finder: preliminary design*. In Christopher J. Evans, Luc Simard & Hideki Takami, editeurs, Ground-based and Airborne Instrumentation for Astronomy VII, volume 10702 of *Society of Photo-Optical Instrumentation Engineers (SPIE) Conference Series*, page 107025X, July 2018.

[Hébrard 08] G. Hébrard, F. Bouchy, F. Pont, B. Loeillet, M. Rabus, X. Bonfils, C. Moutou, I. Boisse, X. Delfosse, M. Desort, A. Eggenberger, D. Ehrenreich, T. Forveille, A. M. Lagrange, C. Lovis, M. Mayor, F. Pepe, C. Perrier, D. Queloz, N. C. Santos, D. Ségransan, S. Udry & A. Vidal-Madjar. *Misaligned spin-orbit in the XO-3 planetary system?* , vol. 488, no. 2, pages 763–770, September 2008.

[Kopparapu 13] Ravi Kumar Kopparapu, Ramses Ramirez, James F. Kasting, Vincent Eymet, Tyler D. Robinson, Suvrath Mahadevan, Ryan C. Terrien, Shawn Domagal-Goldman, Victoria Meadows & Rohit Deshpande. *Habitable Zones around Main-sequence Stars: New Estimates*. , vol. 765, no. 2, page 131, March 2013.

[Krisciunas 97] K. Krisciunas. *Optical Night-Sky Brightness at Mauna Kea over the Course of a Complete Sunspot Cycle*. Publications of the Astronomical Society of the Pacific, vol. 109, page 1181, oct 1997.

[Lovis 10] C. Lovis & D. Fischer. *Radial Velocity Techniques for Exoplanets*. In S. Seager, editeur, Exoplanets, pages 27–53. 2010.

[Mayor 95] M. Mayor & D. Queloz. *A Jupiter - mass companion to a solar - type star*. Nature, vol. 378, page 355, 1995.

[Newman 04] Peter R. Newman, Dan C. Long, Stephanie A. Snedden, S. J. Kleinman, Atsuko Nitta, Michael Harvanek, Jurek Krzesinski, Howard J. Brewington, J. C. Barentine, Eric H. Nielsen Jr. & David J. Schlegel. *Mass-producing spectra: the SDSS spectrographic system*. In Alan F. M. Moorwood & Masanori Iye,

editeurs, Ground-based Instrumentation for Astronomy, volume 5492, pages 533 – 544. International Society for Optics and Photonics, SPIE, 2004.

- [Pepe 02] F. Pepe, M. Mayor, F. Galland, D. Naef, D. Queloz, N. C. Santos, S. Udry & M. Burnet. *The CORALIE survey for southern extra-solar planets VII. Two short-period Saturnian companions to γ ASTROBJ;HD 108147; γ ASTROBJ; and γ ASTROBJ;HD 168746; γ ASTROBJ;.* , vol. 388, pages 632–638, June 2002.
- [Pepe 08] F A Pepe & C Lovis. *From HARPS to CODEX: exploring the limits of Doppler measurements.* Physica Scripta, vol. 2008, no. T130, page 014007, jul 2008.
- [Perryman 14] Michael Perryman, Joel Hartman, Gá spár Á. Bakos & Lennart Lindegren. *ASTROMETRIC EXOPLANET DETECTION WITHiGAIA/i.* The Astrophysical Journal, vol. 797, no. 1, page 14, nov 2014.
- [Pollacco 08] D. Pollacco, I. Skillen, A. Collier Cameron, B. Loeillet, H. C. Stempels, F. Bouchy, N. P. Gibson, L. Hebb, G. Hébrard, Y. C. Joshi, I. McDonald, B. Smalley, A. M. S. Smith, R. A. Street, S. Udry, R. G. West, D. M. Wilson, P. J. Wheatley, S. Aigrain, K. Alsubai, C. R. Benn, V. A. Bruce, D. J. Christian, W. I. Clarkson, B. Enoch, A. Evans, A. Fitzsimmons, C. A. Haswell, C. Hellier, S. Hickey, S. T. Hodgkin, K. Horne, M. Hrudková, J. Irwin, S. R. Kane, F. P. Keenan, T. A. Lister, P. Maxted, M. Mayor, C. Moutou, A. J. Norton, J. P. Osborne, N. Parley, F. Pont, D. Queloz, R. Ryans & E. Simpson. *WASP-3b: a strongly irradiated transiting gas-giant planet.* , vol. 385, no. 3, pages 1576–1584, April 2008.
- [Queloz 01] D. Queloz, G. W. Henry, J. P. Sivan, S. L. Baliunas, J. L. Beuzit, R. A. Donahue, M. Mayor, D. Naef, C. Perrier & S. Udry. *No planet for HD 166435.* Astronomy and Astrophysics, vol. 379, no. 1, pages 279–287, nov 2001.
- [Ramsey 03] Lawrence W. Ramsey, Leland G. Engel, Nicholas Sessions, Christopher De-Filippo, Michelle Graver & Jeffery Mader. *The Hobby-Eberly telescope medium resolution spectrograph and fiber instrument feed.* In Masanori Iye & Alan F. M. Moorwood, editeurs, Instrument Design and Performance for Optical/Infrared Ground-based Telescopes, volume 4841, pages 1036 – 1044. International Society for Optics and Photonics, SPIE, 2003.
- [Ricker 14] George R. Ricker, Joshua N. Winn, Roland Vanderspek, David W. Latham, Gá spár Á. Bakos, Jacob L. Bean, Zachory K. Berta-Thompson, Timothy M.

Brown, Lars Buchhave, Nathaniel R. Butler, R. Paul Butler, William J. Chaplin, David Charbonneau, Jørgen Christensen-Dalsgaard, Mark Clampin, Drake Deming, John Doty, Nathan De Lee, Courtney Dressing, Edward W. Dunham, Michael Endl, Francois Fressin, Jian Ge, Thomas Henning, Matthew J. Holman, Andrew W. Howard, Shigeru Ida, Jon M. Jenkins, Garrett Jernigan, John Asher Johnson, Lisa Kaltenegger, Nobuyuki Kawai, Hans Kjeldsen, Gregory Laughlin, Alan M. Levine, Douglas Lin, Jack J. Lissauer, Phillip MacQueen, Geoffrey Marcy, Peter R. McCullough, Timothy D. Morton, Norio Narita, Martin Paegert, Enric Palle, Francesco Pepe, Joshua Pepper, Andreas Quirrenbach, Stephen A. Rinehart, Dimitar Sasselov, Bun'ei Sato, Sara Seager, Alessandro Sozzetti, Keivan G. Stassun, Peter Sullivan, Andrew Szentgyorgyi, Guillermo Torres, Stephane Udry & Joel Villaseñor. *Transiting Exoplanet Survey Satellite*. *Journal of Astronomical Telescopes, Instruments, and Systems*, vol. 1, no. 1, page 014003, oct 2014.

[Robertson 14] Paul Robertson, Suvrath Mahadevan, Michael Endl & Arpita Roy. *Stellar activity masquerading as planets in the habitable zone of the M dwarf Gliese 581*. *Science*, vol. 345, no. 6195, pages 440–444, July 2014.

[Roy 20] Arpita Roy, Samuel Halverson, Suvrath Mahadevan, Gudmundur Stefansson, Andrew Monson, Sarah E. Logsdon, Chad F. Bender, Cullen H. Blake, Eli Golub, Arvind Gupta, Kurt P. Jaehnig, Shubham Kanodia, Kyle Kaplan, Michael W. McElwain, Joe P. Ninan, Jayadev Rajagopal, Paul Robertson, Christian Schwab, Ryan C. Terrien, Sharon Xuesong Wang, Marsha J. Wolf & Jason T. Wright. *Solar Contamination in Extreme-precision Radial-velocity Measurements: Deleterious Effects and Prospects for Mitigation*. *The Astronomical Journal*, vol. 159, no. 4, page 161, mar 2020.

[Santerne 11a] A. Santerne, A. S. Bonomo, G. Hébrard, M. Deleuil, C. Moutou, J. M. Almenara, F. Bouchy & R. F. Díaz. *SOPHIE velocimetry of Kepler transit candidates. IV. KOI-196b: a non-inflated hot Jupiter with a high albedo*. , vol. 536, page A70, December 2011.

[Santerne 11b] A. Santerne, R. F. Díaz, F. Bouchy, M. Deleuil, C. Moutou, G. Hébrard, A. Eggenberger, D. Ehrenreich, C. Gry & S. Udry. *SOPHIE velocimetry of Kepler transit candidates. II. KOI-428b: a hot Jupiter transiting a subgiant F-star*. , vol. 528, page A63, April 2011.

[Schwab 16] C. Schwab, A. Rakich, Q. Gong, S. Mahadevan, S. P. Halverson, A. Roy, R. C. Terrien, P. M. Robertson, F. R. Hearty, E. I. Levi, A. J. Monson, J. T.

Wright, M. W. McElwain, C. F. Bender, C. H. Blake, J. Stürmer, Y. V. Gurevich, A. Chakraborty & L. W. Ramsey. *Design of NEID, an extreme precision Doppler spectrograph for WIYN*. vol. 9908, page 99087H, August 2016.

[Seager 10] S. Seager. *Exoplanets*. 2010.

[Smee 13] Stephen A. Smee, James E. Gunn, Alan Uomoto, Natalie Roe, David Schlegel, Constance M. Rockosi, Michael A. Carr, French Leger, Kyle S. Dawson, Matthew D. Olmstead, Jon Brinkmann, Russell Owen, Robert H. Barkhouser, Klaus Honscheid, Paul Harding, Dan Long, Robert H. Lupton, Craig Loomis, Lauren Anderson, James Annis, Mariangela Bernardi, Vaishali Bhardwaj, Dmitry Bizyaev, Adam S. Bolton, Howard Brewington, John W. Briggs, Scott Burles, James G. Burns, Francisco Javier Castander, Andrew Connolly, James R. A. Davenport, Garrett Ebelke, Harland Epps, Paul D. Feldman, Scott D. Friedman, Joshua Frieman, Timothy Heckman, Charles L. Hull, Gillian R. Knapp, David M. Lawrence, Jon Loveday, Edward J. Mannery, Elena Malanushenko, Viktor Malanushenko, Aronne James Merrelli, Demitri Muna, Peter R. Newman, Robert C. Nichol, Daniel Oravetz, Kaike Pan, Adrian C. Pope, Paul G. Ricketts, Alaina Shelden, Dale Sandford, Walter Siegmund, Audrey Simmons, D. Shane Smith, Stephanie Snedden, Donald P. Schneider, Mark SubbaRao, Christy Tremonti, Patrick Waddell & Donald G. York. *The Multi-object, Fiber-fed Spectrographs for the Sloan Digital Sky Survey and the Baryon Oscillation Spectroscopic Survey*. , vol. 146, no. 2, page 32, August 2013.

[Wolszczan 92] A. Wolszczan & D. A. Frail. *A planetary system around the millisecond pulsar PSR1257 + 12*. , vol. 355, no. 6356, pages 145–147, January 1992.

[Wright 13] Jason T. Wright, Arpita Roy, Suvrath Mahadevan, Sharon X. Wang, Eric B. Ford, Matt Payne, Brian L. Lee, Ji Wang, Justin R. Crepp, B. Scott Gaudi, Jason Eastman, Joshua Pepper, Jian Ge, Scott W. Fleming, Luan Ghezzi, Jonay I. González-Hernández, Phillip Cargile, Keivan G. Stassun, John Wisniewski, Leticia Dutra-Ferreira, Gustavo F. Porto de Mello, Márcio A. G. Maia, Luiz Nicolaci da Costa, Ricardo L. C. Ogando, Basilio X. Santiago, Donald P. Schneider & Fred R. Hearty. *MARVELS-1: A Face-on Double-lined Binary Star Masquerading as a Resonant Planetary System and Consideration of Rare False Positives in Radial Velocity Planet Searches*. , vol. 770, no. 2, page 119, June 2013.

- [Yan 16] Renbin Yan, Kevin Bundy, David R. Law, Matthew A. Bershady, Brett Andrews, Brian Cherinka, Aleksandar M. Diamond-Stanic, Niv Drory, Nicholas MacDonald, José R. Sánchez-Gallego, Daniel Thomas, David A. Wake, Anne-Marie Weijmans, Kyle B. Westfall, Kai Zhang, Alfonso Aragón-Salamanca, Francesco Belfiore, Dmitry Bizyaev, Guillermo A. Blanc, Michael R. Blanton, Joel Brownstein, Michele Cappellari, Richard D’Souza, Eric Emsellem, Hai Fu, Patrick Gaulme, Mark T. Graham, Daniel Goddard, James E. Gunn, Paul Harding, Amy Jones, Karen Kinemuchi, Cheng Li, Hongyu Li, Roberto Maiolino, Shude Mao, Claudia Maraston, Karen Masters, Michael R. Merrifield, Daniel Oravetz, Kaike Pan, John K. Parejko, Sebastian F. Sanchez, David Schlegel, Audrey Simmons, Karun Thanjavur, Jeremy Tinker, Christy Tremonti, Remco van den Bosch & Zheng Zheng. *SDSS-IV MaNGA IFS Galaxy Survey—Survey Design, Execution, and Initial Data Quality.* , vol. 152, no. 6, page 197, December 2016.
- [Yoachim 16] Peter Yoachim, Michael Coughlin, George Z. Angeli, Charles F. Claver, Andrew J. Connolly, Kem Cook, Scott Daniel, Željko Ivezić, R. Lynne Jones, Catherine Petry, Michael Reuter, Christopher Stubbs & Bo Xin. *An optical to IR sky brightness model for the LSST.* vol. 9910, page 99101A, July 2016.